Mechanismen hochfrequenter synaptischer Übertragung an einer zentralen Synapse

Dissertation
zur Erlangung des akademischen Grades
Dr. med.

an der Medizinischen Fakultät
der Universität Leipzig

eingereicht von:
Andreas Ritzau-Jost, geboren Ritzau
Geboren am 31.10.1989 in Friedrichroda

angefertigt am:
Carl-Ludwig-Institut für Physiologie
Abteilung I
Universitätsklinikum der Universität Leipzig

Betreuer:
Prof. Dr. med. Stefan Hallermann

Beschluss über die Verleihung des Doktorgrades vom 23.08.2016

Inhaltsverzeichnis

Abbildungsverzeichnis

Abkürzungsverzeichnis

AMPA = α-Amino-3-Hydroxy-5-Methyl-4-Isoxazolpropionat

AP = Aktionspotenzial

cMFB = cerebellärer Moosfaserbouton

GABA = γ-Aminobuttersäure

GC = Körnerzelle

Hz = Hertz

kHZ = Kilohertz

GΩ = Gigaohm

MΩ = Megaohm

μm = Mikrometer

ms = Millisekunde

MF = Moosfaser

NMDA = N-Methyl-D-Aspartat

PC = Purkinje-Zelle

ZNS = zentrales Nervensystem

1 Bibliographische Zusammenfassung

Ritzau-Jost, Andreas

Mechanismen hochfrequenter synaptischer Übertragung an einer zentralen Synapse

Universität Leipzig, Dissertation
63 S.[1], 56[2] / 80 Lit.[3], 5 Abb., 0 Tab., 6 Anlagen

Referat:
Die vorliegende Dissertation verfolgt das Ziel, die von Nervenzellen maximal erreichte Signalrate zu bestimmen. Außerdem werden die bislang weitgehend unbekannten Anpassungen einer Synapse an die Anforderungen hochfrequenter Signalübertragung untersucht. Die maximale Übertragungsrate spielt im zentralen Nervensystem eine wichtige Rolle für die Codierung und Verarbeitung von Informationen. Neben den Grundlagen der synaptischen Übertragung und der neuronalen Informationscodierung werden in der Einleitung die anatomischen Gegebenheiten der Kleinhirnrinde und der Moosfaser-Körnerzell-Synapse vorgestellt. Präsynaptische *patch-clamp*-Messungen von Moosfaserboutons und die erstmals durchgeführten Messungen von präsynaptischen Boutons und postsynaptischen Körnerzellen („Paarableitungen“) werden erläutert. Mit Hilfe dieser Methoden wird gezeigt, dass die Kommunikation zwischen Nervenzellen mit Raten von bis zu einem Kilohertz stattfinden kann. Hierbei ist die präsynaptische Freisetzung von Botenstoffen schneller und effizienter als bisher bekannt. Ein einzigartiges Repertoire präsynaptischer Mechanismen wird charakterisiert und bildet die Grundlage der nachgewiesenen, hochfrequenten Informationsübertragung.

---

[1] Seitenzahl insgesamt

[2] Zahl der im Literaturverzeichnis der Einführung ausgewiesenen Literaturangaben

[3] Zahl der im Literaturverzeichnis des Manuskripts ausgewiesenen Literaturangaben

2 Einführung

2.1 Der cerebelläre Cortex und die Moosfaser-Körnerzell-Synapse

Das Kleinhirn (lat. Cerebellum) ist beteiligt an einer Vielzahl motorischer Funktionen, es scheint aber auch bei höheren kognitiven Funktionen eine Rolle zu spielen (Sacchetti *et al.*, 2004; Schmahmann und Caplan, 2006). Die Rinde (lat. Cortex) des Kleinhirns erhält über Moosfasern den Hauptteil der afferenten Signale aus dem zentralen Nervensystem (Abb. 1A). Moosfasern sind Axone von peripheren, sensorischen Neuronen, von Neuronen des Rückenmarks, des Hirnstamms und von intracerebellären Nervenzellen (Ito, 2012). Einzelne Moosfasern verlaufen mehrere Millimeter im cerebellären Cortex (Krieger *et al.*, 1985) und formen über Auftreibungen, den sogenannten cerebellären Moosfaserboutons (cMFB), exzitatorische Synapsen vor allem mit Körnerzellen. Körnerzellen wiederum sind die häufigsten und kleinsten Neuronen des Säugetier-ZNS (Braitenberg und Atwood, 1958; Zagon *et al.*, 1977). Ihre Axone steigen als Parallelfasern in die Molekularschicht des Cortex auf und formen Synapsen unter anderem mit Purkinje-Zellen (Eccles *et al.*, 1967). Die Axone der Purkinje-Zellen verlassen schließlich die Kleinhirnrinde (Abb. 1A) und hemmen Neurone der Kleinhirnkerne.

Die cerebelläre Moosfaser-Körnerzell-Synapse ist die erste und schnellste Station der synaptischen Übertragung auf dem Weg von den Moosfasern über die Körnerzellen zu den Purkinje-Zellen. Auf diesem Weg scheint sich die maximale Frequenz der Übertragung zu verringern (Jörntell und Ekerot, 2006; Rancz *et al.*, 2007; Blot und Barbour, 2014). Moosfasern erreichen verschiedene Kleinhirnwindungen und formen in ihrem Verlauf im Abstand von 20-80 µm Auftreibungen (Palay und Chan-Palay, 1974). Diese sind verglichen mit anderen Präsynapsen außerordentlich groß und komplex geformt (Abb. 1B; Jakab und Hamori, 1988, aber siehe auch Delvendahl *et al.*, 2013) und erregen 20 bis 100 Körnerzellen (Abb. 1C). Körnerzellen als postsynaptische Neurone sind kompakt und haben 3-5 kurze Dendriten (Eccles *et al.*, 1967), die jeweils mit verschiedenen Boutons Synapsen bilden.

Bei der Übertragung zwischen Moosfasern und Körnerzellen bindet der Neurotransmitter Glutamat vorwiegend an α-Amino-3-Hydroxy-5-Methyl-4-Isoxazolpropionat- (AMPA), aber auch an N-Methyl-D-Aspartat- (NMDA) Rezeptoren (Traynelis *et al.*, 1993). Die Neurotransmission erfolgt dabei sowohl direkt, das heißt unmittelbar zwischen der präsynaptischen Freisetzungsstelle von Neurotransmitter und den gegenüberliegenden postsynaptischen Rezeptoren, als auch indirekt. Die indirekte Übertragung ist langsamer und entsteht durch Diffusion von an benachbarten Freisetzungsstellen freigewordenem Neurotransmitter. Sie kann bis zu 50% der übertragenen Ladungen ausmachen und wird als "Überlauf-Strom" bezeichnet (DiGregorio *et al.*, 2002).

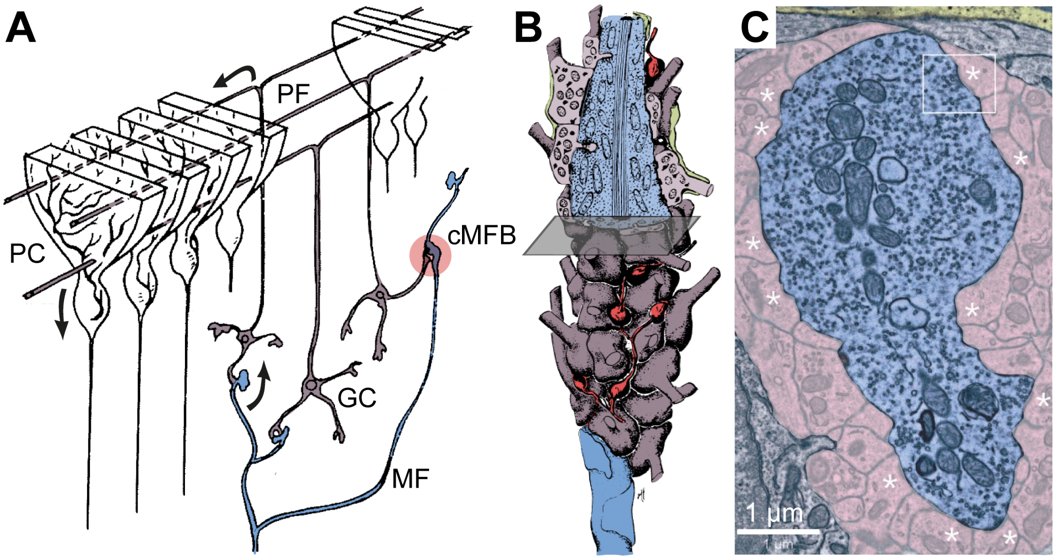

Abb. 1: Vereinfachte schematische Darstellung des cerebellären Cortex und der Moosfaser-Körnerzell-Synapse

A Moosfasern (MF, blau) projezieren über ihre präsynaptischen Auftreibungen (cerebelläre Moosfaserboutons, cMFB) auf eine Vielzahl von Körnerzellen (GC; braun). Das Körnerzell-Axon formt Parallelfasern (PF), die Exzitation an Purkinje-Zellen (PC; weiß) vermitteln. Purkinjezell-Axone projizieren schließlich inhibitorisch auf die tiefen cerebellären Kerngebiete außerhalb des Cortex .

B Darstellung eines *en passent*-Moosfaserboutons (blau), umgeben von dendritischen Fortsätzen postsynaptischer Körnerzellen (braun; vgl. rot unterlegter Bereich in A für die Lokalisation im cerebellären Cortex). Ebenso dargestellt sind die Auftreibungen eines inhibitorischen Golgizell-Axons zwischen den Körnerzelldendriten (rot). Der Anschnitt (obere Bildhälfte) zeigt synaptische Kontakte, sowie die Binnenstruktur des Boutons. Umgebende Gliazell-Fortsätze sind hellgrün dargestellt (Abb. A & B mod. nach Ito, 1984).

C Elektronenmikroskopischer Querschnitt eines cMFB und der umgebenden Körnerzelldendriten (Schnittebene und Farbcode siehe B). Angeschnittene Synapsen sind mit einem Stern gekennzeichnet. (Abb. C mod. nach Xu-Friedman und Regehr, 2003)

Körnerzellen sind tonisch durch γ-Aminobuttersäure (GABA) gehemmt (Brickley *et al.*, 1996; Chadderton *et al.*, 2004). Damit wird die Leitung von zufällig im neuronalen Netzwerk entstehenden Aktionspotenzialen (APs) verhindert und so postsynaptisches Rauschen verringert (Chadderton *et al.*, 2004; Philipona und Coenen, 2004). Hochfrequente AP-Wiederholungen einzelner (Maus; Rancz *et al.*, 2007) oder mehrerer Moosfasern (Katze; Jörntell und Ekerot, 2006) überwinden *in vivo* hingegen die tonische Inhibition und rufen postsynaptisch Ströme hervor.

Die meisten Synapsen übertragen lediglich Frequenzen unter fünfzig APs pro Sekunde (< 50 Hz) zuverlässig (Kandel *et al.*, 2012). In *in vivo*-Experimenten an Katzen zeigen Moosfasern hingegen APs mit außerordentlich hohen Frequenzen bis in den Kilohertz-Bereich (Cooke *et al.*, 1971; Clendenin *et al.*, 1974; Jörntell und Ekerot, 2006). Auch die Stimulation an Tasthaaren der Maus ruft AP-*bursts* (aus wenigen APs bestehende, hochfrequente Repetitionen) in Moosfasern mit bis zu 700 Hz hervor (Abb. 2A; Rancz *et al.*, 2007). Präsynaptische Signale können ohne Informationsverlust mit bis zu 300 Hz auf Körnerzellen übertragen werden (Abb. 2B, C). Ein großer Vorrat von synaptischen Vesikeln und eine beschleunigte Transmitter-Nachladung scheinen dabei eine Rolle zu spielen (Saviane und Silver, 2006). Diese hohen Frequenzen sind erstaunlich vor dem Hintergrund, dass die komplexe synaptische Übertragung dafür hundertfach in Sekundenbruchteilen stattfinden muss. Welche Mechanismen diese hochfrequenten Prozesse auf molekularer Ebene ermöglichen, ist trotz intensiver Forschung ungenügend verstanden.

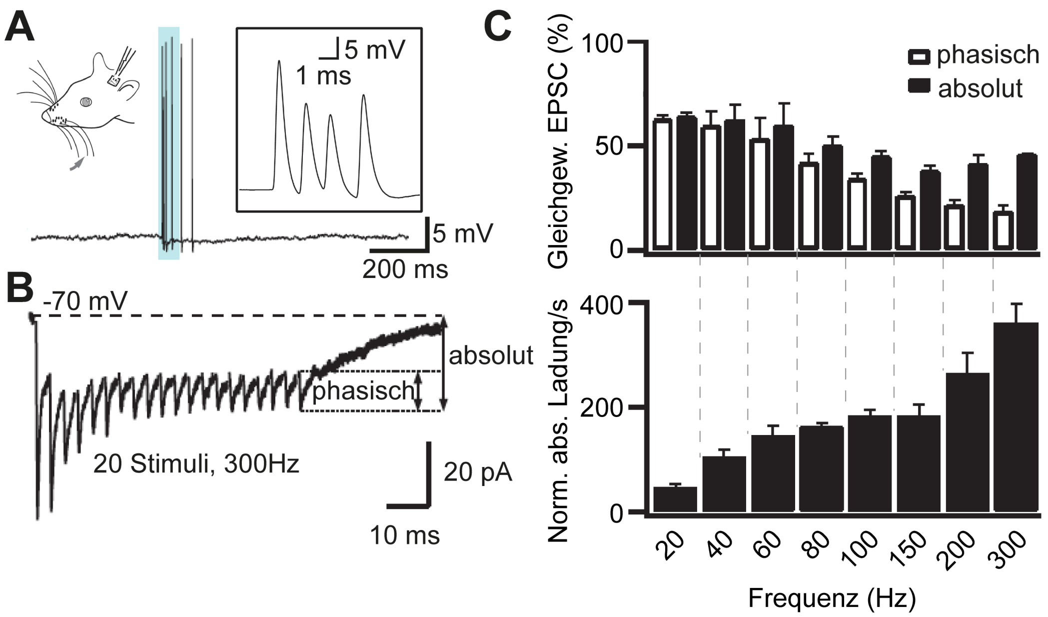

Abb. 2: Hochfrequente Signalübertragung an der Moosfaser-Körnerzell-Synapse

A *In vivo whole-cell* Ableitung von Moosfaserboutons. Durch Tasthaar-Stimulation (siehe schematische Darstellung links) werden AP-*bursts* mit bis zu 700 Hz hervorgerufen (blau hervorgehobener Bereich). Die initialen Aktionspotenziale sind rechts vergrößert dargestellt (Abb. A mod. nach Rancz *et al.*, 2007).

B Durch *in vitro*-Stimulation von Moosfasern hervorgerufene postsynaptische Ströme in Körnerzellen. Jeder der 20 Stimuli wird dabei stabil auf die postsynaptische Zelle übertragen. Der Anteil des phasischen Stroms am Gesamtstrom sinkt im Verlauf der Stimulation, die tonische Komponente nimmt zu. Nach wenigen Stimuli stellt sich ein Gleichgewicht von phasischem und tonischem Strom ein.

C *Oben:* Anteil der phasischen Stromkomponente aus B am Gesamtstrom bei verschiedenen Frequenzen. Im Gleichgewicht sinkt die phasische Komponente verglichen mit dem absoluten postsynaptischen Strom bei höheren Frequenzen. Die auf die postsynaptische Zelle übertragene, absolute Ladung pro Sekunde (als Korrelat der übertragenen Information pro Zeiteinheit) steigt bei Stimulation von 20 bis 300 Hz (Abb. B & C mod. nach Saviane und Silver, 2006).

2.2 Grundlagen der synaptischen Übertragung

Prä- und Postsynapse trennt ein synaptischer Spalt, der zur Signalübertragung zwischen zwei Neuronen überwunden werden muss. Präsynapsen empfangen APs, die über die Öffnung spannungsabhängiger Calciumkanäle einen Einstrom von Calcium-Ionen in das präsynaptische Zellinnere auslösen. Dort bindet Calcium an spezialisierte Proteine, die das Verschmelzen von im Zellinneren vorliegenden Vesikeln mit der Zellmembran bewirken (Chapman, 2008; Südhof, 2012). Der in den Vesikeln gespeicherte Neurotransmitter wird so in den synaptischen Spalt freigesetzt und diffundiert zur Postsynapse. Dort ruft er über Bindung an spezifische Rezeptormoleküle ein elektrochemisches Signal hervor (Katz, 1969), das durch Abbau, durch Diffusion aus dem synaptischen Spalt oder durch Wiederaufnahme des Botenstoffs in die Präsynapse endet (Watkins und Evans, 1981). Die mit der Membran der Präsynapse verschmolzenen Vesikel werden ins Zytosol der Präsynapse retrahiert und erneut mit Neurotransmittern befüllt. Dieser als Endozytose bezeichnete Prozess wirkt einer Vergrößerung der Präsynapse durch stete Vesikelfusion entgegen und erhält, zusammen mit der Rekrutierung von Vesikeln aus Reservepools, den präsynaptischen Vesikelbestand (Royle, 2003). Die gesamte synaptische Übertragung kann innerhalb einer Millisekunde (Wojcik und Brose, 2007) ablaufen und erlaubt verschiedene Mechanismen der Informationscodierung.

2.3 Informationscodierung im Nervensystem

Die Frequenz von APs und deren zeitlicher Bezug codieren die zu verarbeitenden Informationen (Raten- oder Frequenzcodierung versus Zeitcodierung; Rieke *et al.*, 1999; Prescott und Sejnowski, 2008). Während für die Ratencodierung mindestens zwei - in der Regel jedoch weit mehr - APs erforderlich sind, um die Information einer Signalrate (oder Frequenz) zu transportieren, kann bei der Zeitcodierung bereits ein einzelnes AP Träger dieser Information sein. Ratencodierung kann in kurzen Phasen hochfrequenter Repetition (*bursts*, Abb. 2A) mit variablem zeitlichen Bezug zum Stimulus stattfinden. Eine zeitlich präzise Leitung und Verarbeitung der APs ist hingegen Voraussetzung für die zeitliche Codierung. Für beide Mechanismen gibt es zahlreiche experimentelle Nachweise: Codierung durch Signalraten spielt im Cerebellum von Affen bei der Vermittlung von Bewegungsrichtungen von Gliedmaßen eine Rolle (Abbildung 3A, B; van Kan *et al.*, 1993). Einer anderen Studie zufolge (London *et al.*, 2010) garantiert Ratencodierung in der Großhirnrinde der Maus die Robustheit neuronaler Signale gegenüber stochastischem Rauschen, das zeitlich präzise synaptische Ereignisse in komplexeren Netzwerken unwahrscheinlich macht. Die Autoren führen jedoch an, dass der zeitliche Bezug von Stimulus und AP bei schneller Reizänderung und Reizleitung aus der Peripherie ins ZNS von Bedeutung sein kann. Es ist nachgewiesen, dass diese Zeitcodierung bei der Stimulation von Tasthaaren der Maus (Jones *et al.*, 2004) und bei der taktilen Wahrnehmung an der menschlichen Hand (Johansson und Birznieks, 2004) eine Rolle spielt. Auch eine Studie an der cerebellären Moosfaser-Körnerzell-Synapse (D'Angelo und De Zeeuw, 2009) betont die Rolle der Codierung über die Zeit, da wegen einer synchron zur Erregung auftretenden Körnerzell-Hemmung nur kurze Zeitfenster von ca. 5 ms zur Informationsübertragung zur Verfügung stehen. Bei einer angenommenen AP-Frequenz von 100 bis 200 Hz würden dabei zu wenige APs übertragen werden, um zuverlässig eine Signalrate zu codieren.

Eine andere *in vivo* Studie an Mäusen zeigt hingegen, dass Ratencodierung an dieser Synapse von Bedeutung ist (Arenz *et al.*, 2008). In dieser Studie wurden Mäuse horizontal drehbar fixiert (Abb. 3C) und Signale einzelner Körnerzellen abgeleitet (Abb. 3D). Die Frequenz der gemessenen Signale veränderte sich abhängig von der Bewegungsrichtung und deren Geschwindigkeit (Abb. 3D), während sie von der Position und der Beschleunigung der Maus unabhängig war. Die Tatsache, dass Informationen bei hohen Signalraten zuverlässig übertragen werden, spricht für eine große Bandbreite an Frequenzen, die an dieser Synapse zum Codieren von Informationen zur Verfügung stehen. Unklar bleibt, wie schnell synaptische Übertragung maximal und ohne Informationsverlust stattfinden kann. Diese maximale Rate ist kritisch von mehreren Parametern abhängig, beispielsweise der Dauer der einzelnen Aktionspotenziale, aus denen sich die repetitiven Signale zusammensetzen und zwischen denen die Membran ihr Ruhepotenzial erreicht (Bean, 2007; Carter und Bean, 2009; Gittis *et al.*, 2010). Welche Ionenkanal-Subtypen an dieser Synapse rapide AP-Transmission ermöglichen, ist ebenso unbekannt. Auch strukturelle Fragen, beispielsweise nach dem Abstand zwischen präsynaptischen Calciumkanälen und dem Calciumsensor der Vesikel – einem Parameter, der Geschwindigkeit und Effizienz von Synapsen maßgeblich beeinflusst (Bucurenciu *et al.*, 2010; Eggermann *et al.*, 2012; Schmidt *et al.*, 2012; Vyleta und Jonas, 2014) – bleiben bislang ungeklärt.

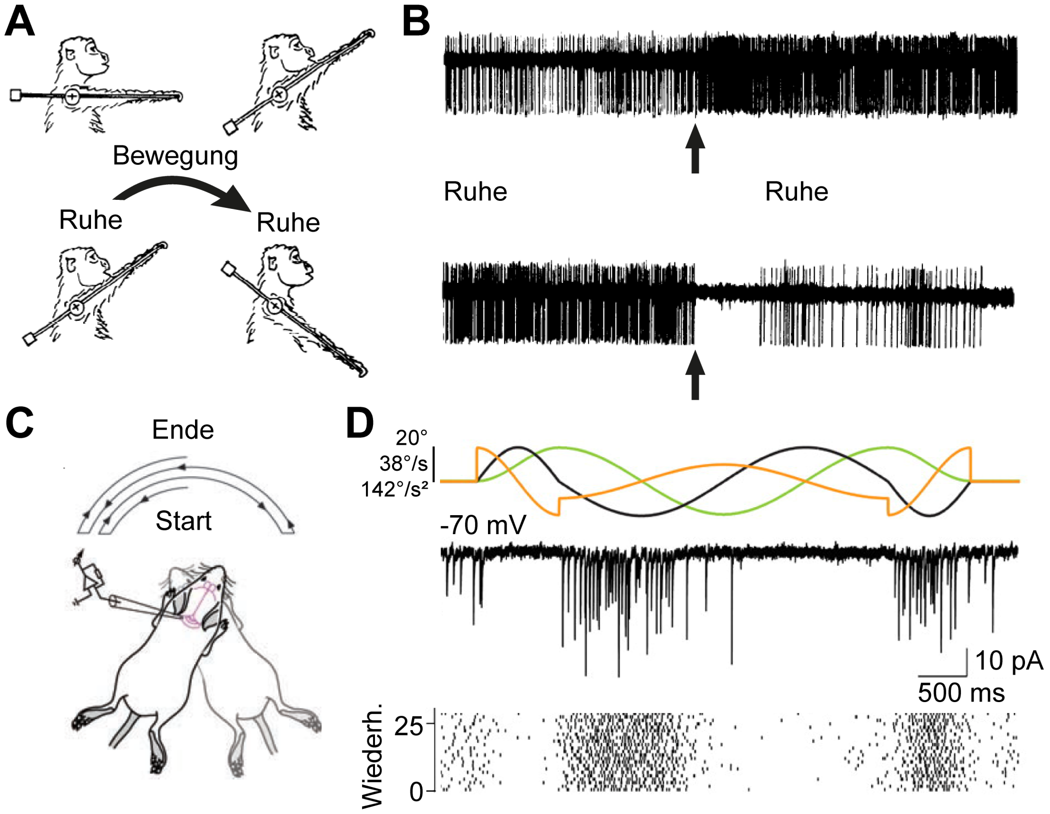

Abb. 3: Frequenzcodierung zwischen Moosfasern und Körnerzellen

A Bewegungsprotokoll eines Affen als gegenläufige Bewegung des fixierten Schultergelenks (oben und unten) zwischen zwei Ruhepositionen.

B Die zeitgleich zu den Bewegungsprotokollen aus A *in vivo* abgeleitete Aktivität einer cerebellären Moosfaser. Der Bewegungsbeginn zwischen beiden Ruhepositionen ist mit einem Pfeil gekennzeichnet. Die Gesamtdauer der Aufzeichnung entspricht ~13 Sekunden. Die Rate der Aktivität verändert sich in Abhängigkeit von der Bewegungsrichtung (Bewegung nach oben erhöht die Frequenz, Bewegung nach unten verringert die Frequenz, Abb. A & B mod. nach van Kan *et al.*, 1993).

C *In vivo*-Messung von Körnerzellaktivität an horizontal drehbar gelagerten Mäusen. Das Bewegungsprotokoll ist als Pfeil dargestellt.

D *Oben*: Position (grün), Bewegungsgeschwindigkeit (schwarz) und Beschleunigung (orange) der Maus während des Protokolls (C). Skalierung von oben nach unten für Position, Geschwindigkeit und Beschleunigung. *Mitte*: Die Rate der postsynaptischen Ströme einer Körnerzelle verändert sich abhängig von Bewegungsgeschwindigkeit und -richtung und ist unabhängig von Position und Beschleunigung. *Unten*: Die Aufzeichnung der Körnerzellaktivität in 28 konsekutiven Messungen zeigt die Stabilität der Aktivitätsmuster (Abb. C & D mod. nach Arenz *et al.*, 2008).

2.4 Etablierung von Ableitungen an der Moosfaser-Körnerzell-Synapse

Um Fragen nach der maximalen Signalfrequenz und den dafür verantwortlichen Mechanismen nachzugehen, wurden Messungen an cerebellären Moosfaserboutons in akuten, 300 µm dicken Kleinhirnschnitten von Mäusen durchgeführt. Mit Hilfe der Infrarot-Differenz-Interferenz-Kontrast-Mikroskopie (IR-DIC-Mikroskopie) wurden Boutons in der Körnerzellschicht des cerebellären Cortex identifiziert. In einigen Experimenten wurden Mäuse genutzt, die fluoreszierende Proteine in einigen ihrer Moosfasern exprimierten.

Für die Messung der präsynaptischen Ströme wurden Elektroden verwendet, die in Glaspipetten installiert wurden. Die Glaspipetten wurden unter Hitze entlang ihrer Längsachse gedehnt, so dass an ihren Spitzen eine Öffnung von ca. 1 µm Durchmesser und einem elektrischen Widerstand von 3 – 10 MΩ entstand. Mit diesen Pipetten wurden dann unter Verwendung der *patch-clamp*-Technik präsynaptische Signale gemessen. Dabei wurde eine Pipette mit Hilfe einer Steuerungseinheit (einem sogenannten Mikromanipulator) in einer Badkammer bewegt (Abbildung 4A), während ein angelegter Überdruck an der Pipette dazu führte, dass ständig Flüssigkeit aus dem Pipetteninneren über die Spitze nach außen trat und die Spitze damit frei von Verunreinigungen hielt (Abbildung 4B). Die Pipette wurde zur Zielzelle bewegt, bis durch den Flüssigkeitsstrom an ihrer Spitze eine Verformung an der Zelloberfläche auftrat (schattiert in Abbildung 4C). Unter Reduzierung des Überdrucks wurde die Pipette an die Zielzelle herangeführt und in unmittelbarer Nähe ein leichter Unterdruck angelegt, um die Zellmembran an die Öffnung der Pipettenspitze zu saugen. Zwischen Pipette und der Zellmembran formte sich dabei eine elektrische Abdichtung mit einem Widerstand im Gigaohm-Bereich (sogenannter *gigaseal*, orange in Abbildung 4D). Zuletzt wurde die Membran an der Pipettenspitze durch kurze Unterdruckpulse perforiert, so dass eine elektrische Verbindung von Zell- und Pipetteninnerem entstand (Abbildung 4E). Über die Elektrode der Pipette konnte dann die Spannung der Zellmembran des Boutons (U_m) gemessen und auf eine bestimmte Kommandospannung (U_c) „geklemmt“ werden.

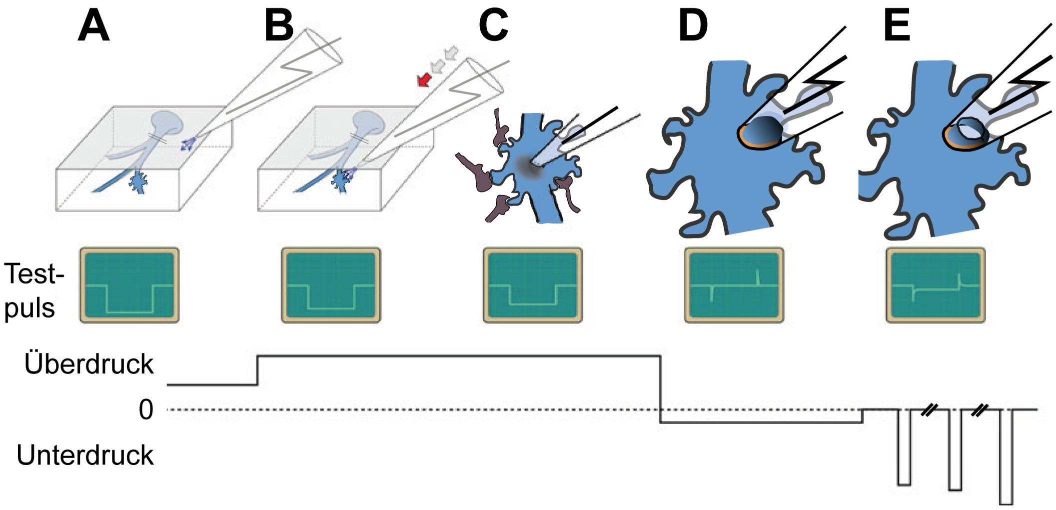

Abb. 4: ***Patch-clamp*-Ableitungen von cerebellären Moosfaserboutons**

A Ein leichter Überdruck und eine Testspannung (Testpuls, -10 mV für 5 ms) wird vor Eintauchen in die Badkammer angelegt.

B Die Pipette wird bei leichtem Überdruck in die Extrazellularlösung getaucht, so dass stetig Flüssigkeit über die Pipettenspitze in die Badperfusion austritt. Gleichzeitig wird die Pipette dem Hirnschnitt angenähert.

C Die Pipettenspitze wird zur Oberfläche eines identifizierten Boutons bewegt, bis diese sich durch den Flüssigkeitsstrom aus der Pipettenspitze verformt.

D Ein leichter Unterdruck wird angelegt, um die Membran des Boutons zur Pipettenspitze zu saugen. Hierbei verringert sich der Strom des Testpulses zunehmend, bis sich eine feste Verbindung der Pipetten- und Boutonoberfläche formt (sogenannter *Gigaseal* aufgrund des entstehenden Abdichtungswiderstandes im GΩ-Bereich) und kein Strom mehr zwischen Pipette und Badkammer fließt (siehe Testpuls).

E Durch kurze Unterdruckpulse wird der Membranfleck oder *patch* unter der Pipettenspitze zerstört. Hierdurch entsteht eine Verbindung zwischen Zellinnerem und dem Inneren der Pipette, über welche die Membranspannung des Boutons geklemmt und eingehende Signale am Bouton abgeleitet werden können (Abb. A – E mod. nach Davie *et al.*, 2006)

Dazu wurde ein Strom (I_{Δ}) proportional zum Spannungsunterschied $\Delta U = U_m - U_c$ in den Bouton geleitet, bis U_m den Wert der Kommandospannung U_c erreichte und damit $\Delta U = 0$ galt. Außerdem konnten Kommandoströme (I_c) in den Bouton geleitet und die daraufhin erzeugte Veränderung des Membranpotenzials gemessen werden. Schließlich ließen sich weitere Parameter, beispielsweise die elektrische Kapazität der Zellmembran, mit hoher zeitlicher Auflösung messen (Lindau und Neher, 1988).

Nach der Etablierung präsynaptischer Messungen an Moosfaserboutons wurde die Möglichkeit von Paarableitungen an der Moosfaser-Körnerzell-Synapse untersucht. Der Begriff „Paarableitung“ bezieht sich hierbei auf das gleichzeitige Messen prä- und postsynaptischer Ströme einer Synapse mit Hilfe der *Patch-clamp*-Technik. Gepaarte Messungen waren zuvor an Modellsynapsen wie der Riesensynapse des Tintenfisches, der Held’schen Calyx im auditorischen Hirnstamm und der Synapse zwischen hippocampalem Moosfaserbouton und der CA3-Pyramidenzelle etabliert worden (Abb. 5; Bullock und Hagiwara, 1957; Borst *et al.*, 1995; Geiger und Jonas, 2000). Dort hatten Paarableitungen zum besseren Verständnis der präsynaptischen Mechanismen beigetragen (Neher und Sakaba, 2001; Sakaba und Neher, 2001b; Lee *et al.*, 2012).

Bei Paarableitungen besteht die Möglichkeit, die Auswirkung präsynaptischer Stimulation direkt am postsynaptischen Neuron zu messen. Das intrazelluläre Milieu der Präsynapse kann dabei durch Hinzufügen verschiedener Substanzen, beispielsweise von Calciumpuffern zur Studie der Calciumkinetik oder spezifischen Proteininhibitoren, verändert und die Auswirkung auf die synaptische Übertragung direkt postsynaptisch registriert werden (Sakaba und Neher, 2001a). Für Experimente mit Paarableitungen wurde zunächst die Ableitung der postsynaptischen Körnerzelle hergestellt. Die für diese Zelle verwendete Intrazellularlösung enthielt einen Fluoreszenzfarbstoff, durch den sich das Körnerzellsoma und dessen Dendriten im Fluoreszenzbild darstellen ließen. Anschließend wurde in der Umgebung der fluoreszierenden Dendriten nach mutmaßlichen Moosfaserboutons gesucht. Diese wurden anhand ihrer charakteristischen elektrophysiologischen Merkmale identifiziert (siehe 6.1. *Supplemental Material*). Ließ sich durch Stimulation der Präsynapse ein stabiler, postsynaptischer Strom hervorrufen, galt die Paarableitung als gesichert.

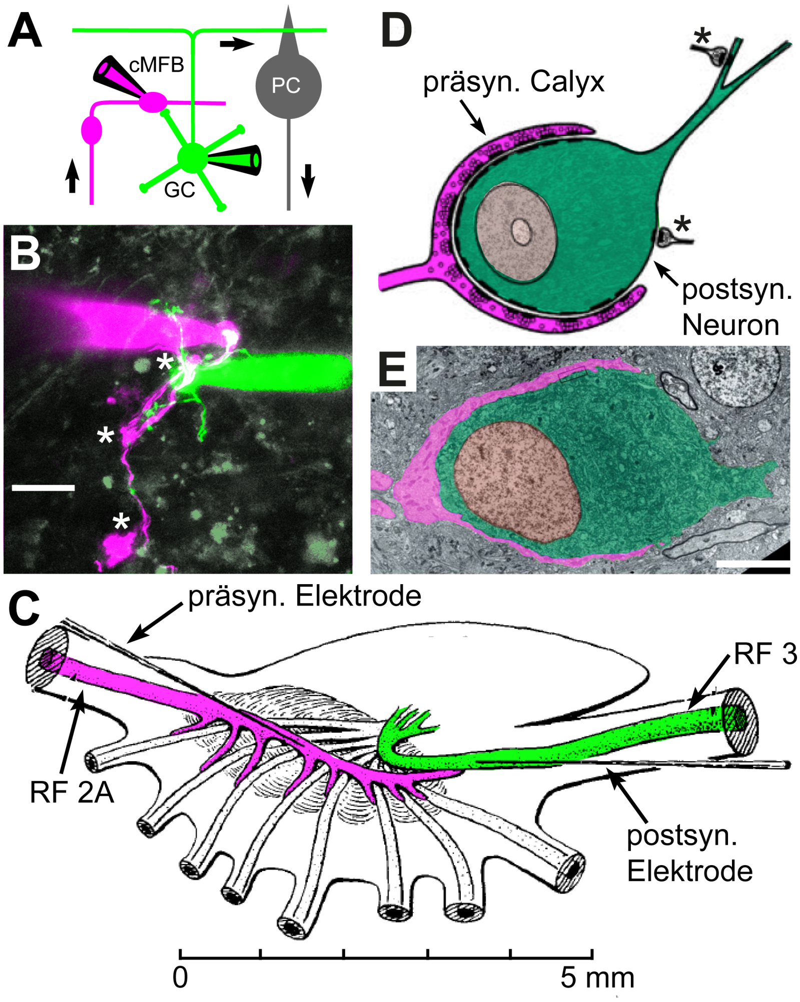

Abb. 5: ***Patch-clamp*****-Paarableitungen an verschiedenen Präparationen**

A Schematische Darstellung der Paarableitung an der Moosfaser-Körnerzell-Synapse im Cerebellum. Die Moosfaser und der präsynaptische cMFB sind in magenta, die Postsynapse (Körnerzelle, GC) in grün dargestellt. Pfeile verdeutlichen den Informationsfluss von Moosfaser über Körnerzelle zur Purkinje-Zelle (PC).

B Fluoreszenzmikroskopische Aufnahme einer Moosfaser-Körnerzell-Synapse während einer Paarableitung (Farbcode wie in A, die beiden mit Fluoreszenzfarbstoff gefüllten Pipetten sind deutlich zu erkennen). Weitere Boutons der selben Moosfaser sind mit Sternen gekennzeichnet. Messbalken 10 µm (Abb. A & B mod. nach Ritzau-Jost *et al.*, 2014).

C Paarableitung an der Riesensynapse des Tintenfisches zwischen Riesenfaser 2A (RF2A, Präsynapse, magenta) und Riesenfaser 3 (RF 3, Postsynapse, grün; Abb. C mod. nach Bullock und Hagiwara, 1957).

D Schematischer Aufbau der Held'schen Calyx. Eine individuelle Präsynapse (Calyx, magenta) bildet die Hauptquelle der Signale des postsynaptischen Neurons im medialen Kern des *Corpus trapezoideum* (grün, Nucleus hellbraun). Weitere erregende und hemmende Synapsen (Sterne) können dabei die Postsynapse beeinflussen.

E Elektronenmikroskopische Aufnahme einer Held'schen Calyx (magenta) und des postsynaptischen Neurons (grün, Nucleus hellbraun). Messbalken 5 µm (Abb. D & E mod. nach Schneggenburger und Forsythe, 2006).

2.5 Quellen der Einführung

Arenz A, Silver RA, Schaefer AT, Margrie TW (2008) The contribution of single synapses to sensory representation *in vivo*. Science 321:977-980.

Bean BP (2007) The action potential in mammalian central neurons. Nat Rev Neurosci 8:451-465.

Blot A, Barbour B (2014) Ultra-rapid axon-axon ephaptic inhibition of cerebellar Purkinje cells by the pinceau. Nat Neurosci 17:289-295.

Borst JG, Helmchen F, Sakmann B (1995) Pre- and postsynaptic whole-cell recordings in the medial nucleus of the trapezoid body of the rat. J Physiol 489:825-840.

Braitenberg V, Atwood RP (1958) Morphological observations on the cerebellar cortex. J Comp Neurol 109:1-33.

Brickley SG, Cull-Candy SG, Farrant M (1996) Development of a tonic form of synaptic inhibition in rat cerebellar granule cells resulting from persistent activation of $GABA_A$ receptors. J Physiol 497:753-759.

Bucurenciu I, Bischofberger J, Jonas P (2010) A small number of open Ca^{2+} channels trigger transmitter release at a central GABAergic synapse. Nat Neurosci 13:19-21.

Bullock TH, Hagiwara S (1957) Intracellular recording from the giant synapse of the squid. J Gen Physiol 40:565-577.

Carter BC, Bean BP (2009) Sodium entry during action potentials of mammalian neurons: Incomplete inactivation and reduced metabolic efficiency in fast-spiking neurons. Neuron 64:898-909.

Chadderton P, Margrie TW, Häusser M (2004) Integration of quanta in cerebellar granule cells during sensory processing. Nature 428:856-860.

Chapman ER (2008) How does synaptotagmin trigger neurotransmitter release? Annu Rev Biochem 77:615-641.

Clendenin M, Ekerot CF, Oscarsson O (1974) The lateral reticular nucleus in the cat. III. Organization of component activated from ipsilateral forelimb tract. Exp Brain Res 21:501-513.

Cooke JD, Larson B, Oscarsson O, Sjolund B (1971) Organization of afferent connections to cuneocerebellar tract. Exp Brain Res 13:359-377.

D'Angelo E, De Zeeuw CI (2009) Timing and plasticity in the cerebellum: focus on the granular layer. Trends Neurosci 32:30-40.

Davie JT, Kole MHP, Letzkus JJ, Rancz EA, Spruston N, Stuart GJ, Häusser M (2006) Dendritic patch-clamp recording. Nat Protoc 1:1235-1247.

Delvendahl I, Weyhersmüller A, Ritzau-Jost A, Hallermann S (2013) Hippocampal and cerebellar mossy fibre boutons - same name, different function. J Physiol 591:3179-88.

DiGregorio DA, Nusser Z, Silver RA (2002) Spillover of glutamate onto synaptic AMPA receptors enhances fast transmission at a cerebellar synapse. Neuron 35:521-533.

Eccles JC, Ito M, Szentágothai J (1967) The Cerebellum as a Neuronal Machine. Berlin: Springer-Verlag.

Eggermann E, Bucurenciu I, Goswami SP, Jonas P (2012) Nanodomain coupling between Ca^{2+} channels and sensors of exocytosis at fast mammalian synapses. Nat Rev Neurosci 13:7-21.

Geiger JRP, Jonas P (2000) Dynamic control of presynaptic Ca^{2+} inflow by fast-inactivating K^+ channels in hippocampal mossy fiber boutons. Neuron 28:927-939.

Gittis AH, Moghadam SH, du Lac S (2010) Mechanisms of sustained high firing rates in two classes of vestibular nucleus neurons: differential contributions of resurgent Na, Kv3, and BK currents. J Neurophysiol 104:1625-1634.

Ito M (1984) The Cerebellum and Neural Control. New York: Raven Press Books, Ltd.

Ito M (2012) The Cerebellum: Brain of an Implicit Self. New Jersey: Pearson Education, Inc.

Jakab RL, Hámori J (1988) Quantitative morphology and synaptology of cerebellar glomeruli in the rat. Anat Embryol (Berl) 179:81-88.

Johansson RS, Birznieks I (2004) First spikes in ensembles of human tactile afferents code complex spatial fingertip events. Nat Neurosci 7:170-177.

Jones LM, Lee S, Trageser JC, Simons DJ, Keller A (2004) Precise temporal responses in whisker trigeminal neurons. J Neurophysiol 92:665-668.

Jörntell H, Ekerot CF (2006) Properties of somatosensory synaptic integration in cerebellar granule cells *in vivo*. J Neurosci 26:11786-11797.

Kandel ER, Schwartz JH, Jessell TM, Siegelbaum SA, Hudspeth AJ (2012) Principles of Neural Science. New York: McGraw Hill Professional.

Katz B (1969) The release of neural transmitter substances. Liverpool, U.K.: Liverpool Univ. Press.

Krieger C, Shinoda Y, Smith AM (1985) Labelling of cerebellar mossy fiber afferents with intra-axonal horseradish peroxidase. Exp Brain Res 59:414-417.

Lee JS, Ho WK, Lee SH (2012) Actin-dependent rapid recruitment of reluctant synaptic vesicles into a fast-releasing vesicle pool. Proc Natl Acad Sci U S A 109:765-774.

Lindau M, Neher E (1988) Patch-clamp techniques for time-resolved capacitance measurements in single cells. Pflügers Arch 411:137-146.

London M, Roth A, Beeren L, Häusser M, Latham PE (2010) Sensitivity to perturbations *in vivo* implies high noise and suggests rate coding in cortex. Nature 466:123-127.

Neher E, Sakaba T (2001) Combining deconvolution and noise analysis for the estimation of transmitter release rates at the calyx of Held. J Neurosci 21:444-461.

Palay SL, Chan-Palay V (1974) Cerebellar Cortex - Cytology and Organization. New York: Springer-Verlag.

Philipona D, Coenen OJMD (2004) Model of granular layer encoding in the cerebellum. Neurocomputing 58–60:575-580.

Prescott SA, Sejnowski TJ (2008) Spike-rate coding and spike-time coding are affected oppositely by different adaptation mechanisms. J Neurosci 28:13649-13661.

Rancz EA, Ishikawa T, Duguid I, Chadderton P, Mahon S, Häusser M (2007) High-fidelity transmission of sensory information by single cerebellar mossy fibre boutons. Nature 450:1245-1248.

Rieke F, Warland D, de Ruyter van Steveninck R, Bialek W (1999) Spikes: Exploring the Neural Code. Cambridge, Massachusetts: The MIT Press

Ritzau-Jost A, Delvendahl I, Rings A, Byczkowicz N, Harada H, Shigemoto R, Hirrlinger J, Eilers J, Hallermann S (2014) Ultrafast action potentials mediate kilohertz signaling at a central synapse. Neuron 84:152-163.

Royle SJ (2003) Endocytosis at the synaptic terminal. J Physiol 553:345-355.

Sacchetti B, Scelfo B, Tempia F, Strata P (2004) Long-term synaptic changes induced in the cerebellar cortex by fear conditioning. Neuron 42:973-982.

Sakaba T, Neher E (2001a) Calmodulin mediates rapid recruitment of fast-releasing synaptic vesicles at a calyx-type synapse. Neuron 32:1119-1131.

Sakaba T, Neher E (2001b) Quantitative relationship between transmitter release and calcium current at the calyx of Held synapse. J Neurosci 21:462-476.

Saviane C, Silver RA (2006) Fast vesicle reloading and a large pool sustain high bandwidth transmission at a central synapse. Nature 439:983-987.

Schmahmann JD, Caplan D (2006) Cognition, emotion and the cerebellum. Brain 129:290-292.

Schmidt H, Brachtendorf S, Arendt O, Hallermann S, Ishiyama S, Bornschein G, Gall D, Schiffmann SN, Heckmann M, Eilers J (2012) Nanodomain coupling at an excitatory cortical synapse. Curr Biol 23:244-249.

Schneggenburger R, Forsythe ID (2006) The calyx of Held. Cell Tissue Res 326:311-337.

Südhof TC (2012) The presynaptic active zone. Neuron 75:11-25.

Traynelis SF, Silver RA, Cull-Candy SG (1993) Estimated conductance of glutamate receptor channels activated during EPSCs at the cerebellar mossy fiber-granule cell synapse. Neuron 11:279-289.

van Kan PL, Gibson AR, Houk JC (1993) Movement-related inputs to intermediate cerebellum of the monkey. J Neurophysiol 69:74-94.

Vyleta NP, Jonas P (2014) Loose coupling between Ca^{2+} channels and release sensors at a plastic hippocampal synapse. Science 343:665-670.

Watkins JC, Evans RH (1981) Excitatory amino acid transmitters. Annu Rev Pharmacol Toxicol 21:165-204.

Wojcik S, Brose N (2007) Regulation of membrane fusion in synaptic excitation-secretion coupling: Speed and accuracy matter. Neuron 55:11-24.

Xu-Friedman MA, Regehr WG (2003) Ultrastructural contributions to desensitization at cerebellar mossy fiber to granule cell synapses. J Neurosci 23:2182-2192.

Zagon IS, McLaughlin PJ, Smith S (1977) Neural populations in the human cerebellum: estimations from isolated cell nuclei. Brain Res 127:279-282.

3 Ziele der Arbeit

Informationen können im zentralen Nervensystem an einigen Synapsen sehr hochfrequent übertragen werden. Hohe Signalraten sind dabei für die Codierung neuronaler Information von Bedeutung. Die Moosfaser-Körnerzell-Synapse bietet geeignete Bedingungen, um die Mechanismen hochfrequenter Signalübertragung zu untersuchen. In einer Studie wurden 2007 erstmals *in vivo* Ableitungen von cerebellären Moosfaserboutons durchgeführt (Rancz *et al.*, 2007), bei denen Signalraten von bis zu 700 Hz registriert wurden. Welche synaptischen Mechanismen bei hohen Signalraten eine Rolle spielen und wie schnell Synapsen maximal aktiv sein können, ist bislang unzureichend verstanden. Es sollte deshalb getestet werden:

1. Mit welcher Frequenz Aktionspotenziale in Boutons maximal hervorgerufen werden können.
2. Wie sich die Kinetik der Aktionspotenziale bei hohen Raten verändert.
3. Inwieweit die präsynaptische Freisetzung von Neurotransmitter den hohen Aktionspotenzial-Frequenzen folgen kann.
4. Welche Natrium-, Kalium- und Calciumströme den Aktionspotenzialen zu Grunde liegen und welche Kinetik diese Ionenströme haben.
5. Ob eine einheitliche oder verschiedene Vesikelpopulationen für die Freisetzung von Botenstoffen verantwortlich sind und wie schnell diese an die Freisetzungsstelle der Präsynapse rekrutiert werden.

Hierfür sollten direkte Messungen von cMFBs in unserem Labor etabliert werden. Um die Auswirkung präsynaptischer Vorgänge direkt am postsynaptischen Partner zu messen, sollten zudem erstmals Paarableitungen an dieser Synapse durchgeführt werden.

4 Publikationsmanuskript

Please cite this article in press as: Ritzau-Jost et al., Ultrafast Action Potentials Mediate Kilohertz Signaling at a Central Synapse, Neuron (2014), http://dx.doi.org/10.1016/j.neuron.2014.08.036

Neuron
Article

CellPress

Ultrafast Action Potentials Mediate Kilohertz Signaling at a Central Synapse

Andreas Ritzau-Jost,[1,2,5] Igor Delvendahl,[1,2,5] Annika Rings,[1,2,5] Niklas Byczkowicz,[1,2] Harumi Harada,[3] Ryuichi Shigemoto,[3] Johannes Hirrlinger,[1,4] Jens Eilers,[1] and Stefan Hallermann[1,2,*]
[1]Carl-Ludwig-Institute for Physiology, Medical Faculty, University of Leipzig, Liebigstr. 27, 04103 Leipzig, Germany
[2]European Neuroscience Institute Göttingen, Grisebachstr. 5, 37077 Göttingen, Germany
[3]Institute of Science and Technology Austria, 3400 Klosterneuburg, Austria
[4]Department of Neurogenetics, Max-Planck-Institute for Experimental Medicine, Hermann-Rein-Strasse 3, 37075 Göttingen, Germany
[5]Co-first author
*Correspondence: hallermann@medizin.uni-leipzig.de
http://dx.doi.org/10.1016/j.neuron.2014.08.036

SUMMARY

Fast synaptic transmission is important for rapid information processing. To explore the maximal rate of neuronal signaling and to analyze the presynaptic mechanisms, we focused on the input layer of the cerebellar cortex, where exceptionally high action potential (AP) frequencies have been reported in vivo. With paired recordings between presynaptic cerebellar mossy fiber boutons and postsynaptic granule cells, we demonstrate reliable neurotransmission up to ∼1 kHz. Presynaptic APs are ultrafast, with ∼100 μs half-duration. Both K_{v1} and K_{v3} potassium channels mediate the fast repolarization, rapidly inactivating sodium channels ensure metabolic efficiency, and little AP broadening occurs during bursts of up to 1.5 kHz. Presynaptic $Ca_v2.1$ (P/Q-type) calcium channels open efficiently during ultrafast APs. Furthermore, a subset of synaptic vesicles is tightly coupled to Ca^{2+} channels, and vesicles are rapidly recruited to the release site. These data reveal mechanisms of presynaptic AP generation and transmitter release underlying neuronal kHz signaling.

INTRODUCTION

Information can be encoded by neural activity as the rate of action potentials (APs) (Arenz et al., 2008; London et al., 2010) and by correlations in spike timing (Rieke et al., 1997). The propagation speed of rate-coded information within a population of neurons is limited by the number of neurons and by the maximal AP frequency of each individual neuron (Rieke et al., 1997; Tchumatchenko et al., 2011). In turn, the maximal sustainable frequency of each neuron is ultimately limited by the duration of the AP (Bean, 2007; Gittis et al., 2010; Lien and Jonas, 2003; Rudy and McBain, 2001). Therefore, the AP duration is a crucial parameter limiting the speed of information processing.

Cerebellar mossy fibers represent one of the main inputs to the cerebellum and send broad-bandwidth signals to the cerebellar cortex with firing frequencies up to 1.2 kHz in vivo (Garwicz et al., 1998; Jörntell and Ekerot, 2006; Rancz et al., 2007). These high-frequency signals are conveyed to granule cells (GCs), the most abundant neurons in the entire brain. In order to connect to the large number of GCs, cerebellar mossy fibers form several collaterals and contain numerous presynaptic boutons along the myelinated axon. In addition, each cerebellar mossy fiber bouton (cMFB) contacts more than 10 GCs (Billings et al., 2014; Jakab and Hámori, 1988). Despite the high degree of divergence at cMFBs, signal transduction to the postsynaptic partners is very efficient (Chadderton et al., 2004; Jörntell and Ekerot, 2006; Rancz et al., 2007; Saviane and Silver, 2006). In a seminal study, Rancz and coworkers (2007) pioneered direct whole-cell patch-clamp recordings from cMFBs in vitro and in vivo, offering the opportunity to directly investigate the mechanisms of high-frequency signaling from single nerve terminals to a large number of postsynaptic partners.

Here, we establish paired patch-clamp recordings between cMFBs and GCs in acute cerebellar brain slices in combination with high-resolution analysis of presynaptic mechanisms. We focus on the properties of APs in cMFBs enabling kHz signaling and the mechanisms by which cMFBs can reliably release neurotransmitter to dozens of GCs. Our recordings demonstrate reliable neurotransmission at frequencies of up to ∼1 kHz and reveal a surprisingly short duration of APs, which is more than 2-fold shorter than previous estimates at central neurons or axons. Furthermore, we show that efficient opening of presynaptic Ca^{2+} channels, tight coupling of vesicles to Ca^{2+} channels, and rapid vesicle recruitment sustain reliable neurotransmitter release during kHz signaling.

RESULTS

Kilohertz Transmission at Single cMFB-GC Connections

Synaptic transmission of individual cMFB-GC connections was analyzed with paired whole-cell patch-clamp recordings from cMFBs and GCs in acute cerebellar brain slices of mature mice at physiological temperatures (schematically illustrated in Figure 1A). Recordings from cMFBs were obtained with the aid of two-photon targeted patching (Margrie et al., 2003) in transgenic mice expressing yellow fluorescent protein in a subset of mossy fibers (Figure 1B; Hirrlinger et al., 2005) or with differential interference contrast microscopy in wild-type mice. For an

Please cite this article in press as: Ritzau-Jost et al., Ultrafast Action Potentials Mediate Kilohertz Signaling at a Central Synapse, Neuron (2014), http://dx.doi.org/10.1016/j.neuron.2014.08.036

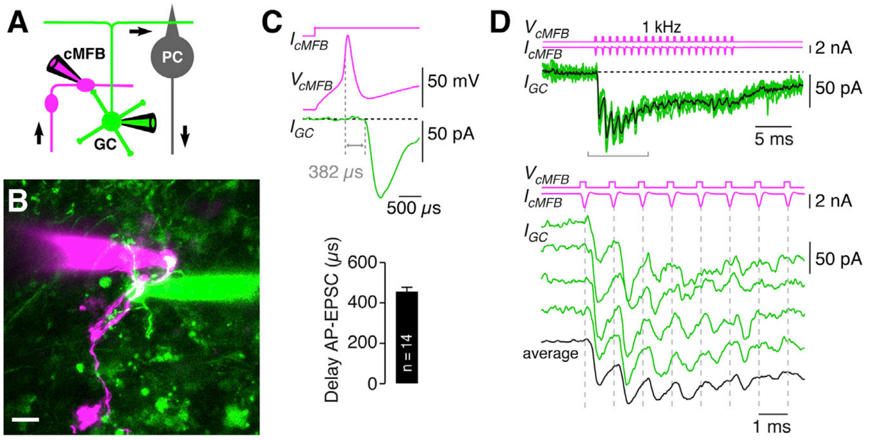

Figure 1. Kilohertz Transmission at Single cMFB-GC Connections

(A) Schematic illustration of the cellular connectivity within the cerebellar cortex. Mossy fibers (magenta) send information to the cerebellar cortex. Presynaptic cerebellar mossy fiber boutons (cMFB) transmit signals to postsynaptic granule cells (GCs, green), which excite Purkinje cells (PC, gray) via parallel fibers. Axons of Purkinje cells represent the sole output of the cerebellar cortex. Two patch-clamp pipettes illustrate the paired cMFB-GC recording configuration.

(B) Two-photon microscopic image of a paired whole-cell patch-clamp recording between a cMFB (magenta) and a GC (green) filled with the fluorescence dyes Atto 594 and Atto 488, respectively, in an acute cerebellar brain slice of a 39-day-old TgN(Thy1.2-EYFP) mouse expressing EYFP in a subset of mossy fibers (green; maximal z-projection of a stack of images over 45 μm; z-step 3 μm). Scale bar, 10 μm.

(C) Top: Example trace of a paired cMFB-GC recording with current injection (I_{cMFB}) evoking an AP in the cMFB (V_{cMFB}) and an EPSC in the postsynaptic GC (I_{GC}). The synaptic delay is indicated. Bottom: Average synaptic delay of n = 14 paired recordings (mean ± SEM).

(D) Top: Voltage clamp of a cMFB with 20 AP-like depolarizations (V_{cMFB}; 200 μs to 0 mV) at a frequency of 1 kHz evoked presynaptic action currents in the cMFB (I_{cMFB}) and EPSCs in the connected GC (four consecutive trials in green, average in black). Bottom: the first seven EPSCs on an expanded scale (cf. bracket in top panel, dashed lines are set to the peak of the action currents; see also Figure S1).

unequivocal identification of cMFBs, we determined the characteristic morphological and electrophysiological properties (see Supplemental Experimental Procedures; Figure S1; Rancz et al., 2007). Brief current injection into cMFBs evoked an AP in the cMFB and an excitatory postsynaptic current (EPSC) in a synaptically connected GC with a synaptic delay of 457 ± 20 μs (n = 14; Figure 1C). To directly analyze transmission in the kHz regime, presynaptic stimulation with 20 AP-like depolarizations (0 mV, 200 μs duration) at a frequency of 1 kHz was used to evoke presynaptic action currents in cMFBs. These presynaptic kHz bursts evoked EPSCs in GCs, consisting of a phasic EPSC, which is related to direct release onto the GC, and a tonic component, part of which is probably due to glutamate spillover from neighboring release sites onto the recorded GC (Figure 1D; DiGregorio et al., 2002). In the example shown in Figure 1D, the average phasic steady-state amplitude of the last ten EPSCs was 8.1 pA. When taking into account the previously reported reduction in EPSC amplitude due to postsynaptic depression of ~30% and the miniature EPSC amplitude of 17 pA (Hallermann et al., 2010), this corresponds to release of about one vesicle each millisecond in this cMFB-GC connection (see below for detailed analysis of the rate of vesicle recruitment). This example demonstrates that a single cMFB-GC connection can reliably transmit information during short bursts at a frequency of 1 kHz.

Ultrafast APs in cMFBs

In order to understand the mechanisms of high-frequency burst signaling, we next analyzed the properties of presynaptic APs. Upon current injection, cMFBs fired APs with durations at half-maximal amplitude of 107 ± 4 μs (n = 44; referred to as half-duration in the following; Figure 2B). To analyze APs undisturbed by a presynaptic depolarization, cMFBs and the adjacent axon were filled with a fluorescent dye (Figure 2A) and a distal part of the axon was approached with a stimulation pipette. We systematically compared APs elicited by current injection and axonal stimulation. The half-duration of APs elicited in the same cMFB was not significantly different between the two modes of AP generation (n = 10, p = 0.1, Wilcoxon signed-rank test; Figure 2C). These data demonstrate that APs of cMFBs are ultrafast with a half-duration of ~100 μs.

To gain insights into the mechanisms allowing such short AP half-duration, we analyzed which K^+ channel subtypes are responsible for AP repolarization. Focal application of the K_{v3} channel gating modifier BDS-I (3 μM; Martina et al., 2007) prolonged AP half-duration to 202 ± 14 μs (n = 11, $p < 0.001$, Mann-Whitney U test), whereas bath application of the K_{v1} channel blocker α-dendrotoxin (DTX, 0.2 mM) prolonged the half-duration to 265 ± 27 μs (n = 11, $p < 0.001$, Mann-Whitney U test; Figures 2D, 2E, and S2). The impact of K_{v3} channels could be underestimated in these experiments because of incomplete focal application of BDS-I or the fact that BDS-I only slows gating but does not block K_{v3} completely (Martina et al., 2007). However, bath application of 1 mM TEA, which blocks $K_{v1.1}$ and all K_{v3} channel subtypes (Gutman et al., 2005), did not have a stronger effect on AP half-duration than focal BDS-I application (p = 0.75; Mann-Whitney U test; Figure 2E). This finding indicates that BDS-I application was successful and that the slowing of the K_{v3} activation kinetics by BDS-I (Martina et al., 2007) corresponds to a complete K_{v3} block during the duration of our APs. Finally, application of 5 mM 4-AP, which blocks K_{v1} and K_{v3} channels, resulted in APs with half-durations of ~1 ms (n = 5, $p < 0.001$, Mann-Whitney U test; Figures 2D and 2E). Although we have not addressed K_{v2} and K_{v4} channels specifically, a strong contribution to the AP repolarization is unlikely, because K_{v2} channels activate slowly and contribute only to repolarization of longer APs (Liu and Bean, 2014), and K_{v4} channels have been shown to localize preferentially to somata and dendrites (Sheng et al., 1992). These data indicate that primarily K^+ channels of the K_{v1} and the K_{v3} channel families mediate the repolarization of ultrafast cMFB APs.

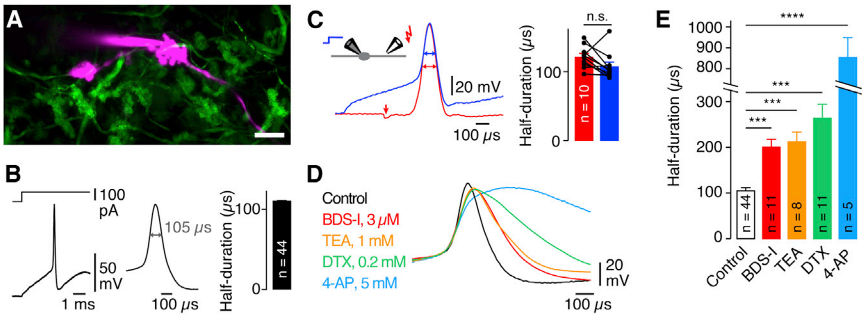

Figure 2. Ultrafast APs in cMFBs

(A) Two-photon image of a whole-cell patch-clamped cMFB and the adjacent axon (magenta; Atto 594 in the pipette solution) in an acute cerebellar brain slice of a 48-day-old TgN(Thy1.2-EYFP) mouse with EYFP-labeled mossy fibers (green; maximal z-projection of a stack of images over 20 μm; z-step 1 μm). Scale bar, 10 μm.

(B) Example of an AP recorded in a cMFB evoked by current injection. Middle: Same example on an expanded time scale (AP half-duration is indicated). Right: Average AP half-duration elicited by current injection (mean ± SEM; n refers to the number of cMFBs).

(C) Left: Comparison of APs elicited by current injection (blue) and axonal stimulation with a second pipette (red) in the same cMFB as illustrated by the color code of the inset. Example APs elicited in both ways are superimposed (arrow indicates stimulation artifact). Right: Comparison between the AP half-duration elicited by axonal stimulation (red) and current injection (blue) in the same cMFBs (mean ± SEM; connected dots represent results from the two stimulation conditions in the same cMFB).

(D) Examples of cMFB APs measured in the presence of indicated K^+ channel blockers. APs were evoked by current injection. Voltage traces are aligned to the AP threshold.

(E) Average AP half-duration after application of the indicated K^+ channel blockers (mean ± SEM). Asterisks indicate significance as described in the text (see also Figure S2).

Fast Inactivating Na^+ and Activating K^+ Channels Generate Ultrafast and Metabolically Efficient APs

We next applied an AP waveform (measured in cMFBs with axonal stimulation) as voltage command to outside-out patches from cMFBs to analyze the Na^+ and K^+ currents underlying the fast cMFB APs. The pharmacologically isolated currents had very short half-durations of 73 ± 9 μs (n = 6) and 61 ± 2 μs (n = 5; Figures 3A and 3B) for Na^+ and K^+, respectively. Metabolic efficiency was quantified as the Na^+ excess ratio, defined as the total Na^+ influx (Na^+ current integrated over the entire duration of the AP) divided by the Na^+ flux until the time of the AP peak (Figure 3C). The Na^+ excess ratio was 1.76 ± 0.12 (n = 6), which is efficient compared with APs of short duration at other preparations (Carter and Bean, 2009, 2011).

To analyze the mechanisms that generate ultrafast but metabolically efficient APs, we studied the kinetic parameters of Na^+ and K^+ currents. Step-depolarizations from −80 to 0 mV applied to outside-out patches revealed rapid Na^+ channel inactivation with a time constant of 81 ± 3 μs (n = 5; Figure 3D), which is consistent with corresponding recordings from axons of fast-spiking interneurons at room temperature, assuming a Q_{10} temperature coefficient of 2.6 (time constant ~300 μs; Hu and Jonas, 2014). Maximally activating voltage steps from −80 to +40 mV were applied to investigate the kinetics of K^+ currents at cMFBs. The activation time constant was 225 ± 24 μs (n = 12; Figure 3E), which is consistent with previous studies of rapidly activating K^+ channels (Martina et al., 2007). Thus, rapid inactivation of Na^+ and activation of K^+ channels underlie efficient cMFB APs.

In order to further dissect whether the kinetics or rather the density of Na^+ and K^+ channels cause the short half-duration of the APs, we estimated current densities from outside-out patches and performed Hodgkin-Huxley modeling based on the measured gating kinetics (Figure S3; see Supplemental Experimental Procedures). However, with the estimated Na^+ and K^+ conductance ($\bar{g}_{Na}$ = 722 and $\bar{g}_K$ = 82 pS · μm^{-2}), the model predicted a too-long half-duration (Figure S3E). To obtain the measured half-duration, a ~10-fold higher K^+ current density was required. An inhomogeneous distribution of K^+ channels could explain this finding (see Discussion). Thus, our approach of high-resolution kinetic analysis of Na^+ and K^+ currents in combination with Hodgkin-Huxley modeling provides indirect evidence for an inhomogeneous distribution of K^+ channels and indicates a high density of Na^+ channels.

Stable APs during kHz Bursts

We evoked presynaptic APs by axonal stimulation at increasing rates (250–2,000 Hz) to analyze the AP shape during high-frequency firing. cMFBs were capable of firing failure-free trains of APs at exceptionally high frequencies (Figure 4A). In the illustrated example, failure-free trains of APs were elicited at up to 1.6 kHz and had almost constant amplitude and half-duration up to 1 kHz (Figures 4A and 4B), suggesting a rapid recovery from sodium channel inactivation (Leão et al., 2005). At frequencies close to the maximal failure-free frequency, slight amplitude reduction and broadening occurred, which fully recovered within a few tens of milliseconds (Figure 4B). Interestingly, the maximal failure-free AP frequency correlated with the AP half-duration (Figure 4C). On average, failure-free frequency for 11 APs was 1.0 ± 0.1 kHz (n = 10; Figure 4D). At the frequency tested before the maximal failure-free frequency (mean 800 ± 89.8 Hz), last AP half-duration was 111 ± 2.5%, and AP amplitude 95.1 ± 1.7% of the first AP (n = 10). These data are similar to findings obtained at the calyx of Held (Wang and Kaczmarek, 1998) and at cMFBs in vivo (Rancz et al., 2007). In contrast, nerve terminals operating at lower frequencies, such as hippocampal mossy fiber boutons, exhibit pronounced AP broadening even at frequencies of 1–100 Hz (Geiger and Jonas, 2000). Thus, cMFBs can generate APs at kHz frequencies with little amplitude reduction and broadening.

Efficient Opening of Ca^{2+} Channels during cMFB APs

In order to understand the mechanisms of synaptic transmission at these frequencies, we next investigated whether the ultrafast APs in cMFBs can reliably open Ca^{2+} channels. With optimized recording conditions (see Supplemental Experimental Procedures), AP-evoked Ca^{2+} currents (Borst and Sakmann, 1998)

Please cite this article in press as: Ritzau-Jost et al., Ultrafast Action Potentials Mediate Kilohertz Signaling at a Central Synapse, Neuron (2014), http://dx.doi.org/10.1016/j.neuron.2014.08.036

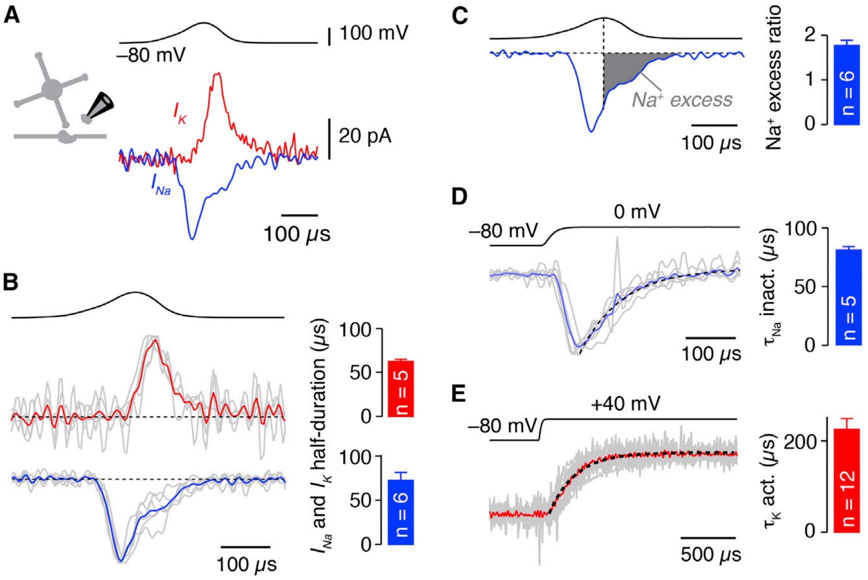

Figure 3. Fast Inactivating Na^+ and Activating K^+ Channels Generate Ultrafast and Metabolically Efficient APs

(A) Examples of pharmacologically isolated Na^+ (blue) and K^+ currents (red) in two different outside-out patches from cMFBs, elicited by a previously recorded AP voltage command (top). Traces are averages of 82 and 101 sweeps for Na^+ and K^+ currents, respectively. Inset: Schematic illustration of the recording configuration.

(B) Superposition of peak normalized AP-evoked currents (gray traces; n = 6 for Na^+, n = 5 for K^+; n represents number of outside-out patches) with the corresponding grand averages (Na^+, blue; K^+, red). Right: Average half-duration of AP-evoked Na^+ (blue) and K^+ current (red; mean ± SEM).

(C) Average AP-evoked Na^+ current. Filled gray area indicates the excess Na^+ influx following the peak of the AP. Right: Average Na^+ excess ratio calculated as total Na^+ influx divided by the Na^+ influx until the time of the AP peak (mean ± SEM).

(D) Superposition of peak normalized Na^+ currents (n = 5, gray) elicited by 3 ms depolarization from −80 mV to 0 mV with the grand average (blue) and an exponential fit to the time course of inactivation (black dashed line). Right: Average time constant of inactivation (mean ± SEM).

(E) Superposition of peak normalized K^+ currents (n = 12, gray) evoked by 3 ms depolarizations from −80 mV to +40 mV with the grand average (red) and an exponential fit to the time course of activation (black dashed line). Right: Average time constant of activation (mean ± SEM; see also Figure S3).

could be resolved having an amplitude of 543 ± 62 pA and a half-duration of 99 ± 4 µs (n = 9; Figure 5A). To determine the relative open probability of Ca^{2+} channels during an AP, Ca^{2+} currents were elicited by AP-like depolarizations of variable duration (Figure 5B). On average, 59% of the available Ca^{2+} current was recruited during an AP (Figure 5C). To understand the efficient opening during short APs, we measured the kinetics of Ca^{2+} currents in cMFBs and found rapid activation and deactivation (Figures S4A and S4B). A two-gate Hodgkin-Huxley model based on the measured activation and deactivation kinetics (Figure S4C) reproduced the AP-evoked Ca^{2+} current (Figure 5A) and predicted a relative open probability of 77% during an AP. Thus, rapid kinetics of presynaptic Ca^{2+} channels can explain the efficient opening of Ca^{2+} channels during short APs at cMFBs.

$Ca_v2.1$ Ca^{2+} Channels at Active Zones of cMFBs

To identify the molecular identity of the presynaptic Ca^{2+} channels at cMFBs, whole-cell Ca^{2+} currents were recorded during application of specific Ca^{2+} channel blockers (Figure 6A). ω-Agatoxin (0.5 µM), which selectively blocks $Ca_v2.1$ (P/Q-type) Ca^{2+} channels, inhibited 70.8% ± 4.3% (n = 10) of the Ca^{2+} current. In contrast, 1 µM ω-Conotoxin, which blocks $Ca_v2.2$ (N-type) Ca^{2+} channels, and 0.5 µM SNX-482, which blocks $Ca_v2.3$ (R-type) Ca^{2+} channels, inhibited only 15.5% ± 2.8% (n = 11) and 11.9% ± 1.8% (n = 5) of the Ca^{2+} current, respectively (Figure 6B). Thus, $Ca_v2.1$ Ca^{2+} channels mediate the majority of the Ca^{2+} current at cMFBs. To investigate whether these channels are localized at the active zone, we analyzed the localization of $Ca_v2.1$ Ca^{2+} channels using pre-embedding immunogold labeling for $Ca_v2.1$ in mice (Indriati et al., 2013). Immunogold particles for $Ca_v2.1$ were often found in the presynaptic active zone of cMFBs making synapses onto granule cell dendrites (Figure 6C). The density of particles was ~50 times higher at the active zone compared with extrasynaptic membrane (Figure 6D). Consistently, freeze-fracture replica labeling of cerebellar granule cell layer also showed clustered $Ca_v2.1$ Ca^{2+} channels at putative active zones of cMFBs (Figure 6E). These data indicate that $Ca_v2.1$ Ca^{2+} channels, which are clustered at active zones, represent the majority of Ca^{2+} channels at cMFBs.

Measuring Vesicular Release Simultaneously from Presynaptic Capacitance Increase and Postsynaptic Currents

To understand how the brief Ca^{2+} influx can elicit synchronous release during kHz bursts, we next analyzed fundamental parameters of release, such as the number of release-ready vesicles, the speed of vesicle recruitment, and the vesicle to Ca^{2+} channel coupling distance. We combined two independent techniques to measure these parameters in the paired-recording configuration: presynaptic capacitance measurements and deconvolution of postsynaptic currents (Sakaba, 2006; Sun and Wu, 2001; von Gersdorff et al., 1998; Wölfel et al., 2007). Depolarizing pulses of increasing duration (0 mV; 1–100 ms) were applied to the presynaptic terminal (Figure 7A). The presynaptic Ca^{2+} current, the induced capacitance increase due to vesicle exocytosis, and the evoked postsynaptic current were measured simultaneously. Deconvolution of postsynaptic currents led to an estimate of presynaptic release rates during the pulses (Figure 7A; see Supplemental Experimental Procedures). The capacitance increase and the number of vesicles estimated by deconvolution scaled linearly for depolarizations of 1–100 ms

Please cite this article in press as: Ritzau-Jost et al., Ultrafast Action Potentials Mediate Kilohertz Signaling at a Central Synapse, Neuron (2014), http://dx.doi.org/10.1016/j.neuron.2014.08.036

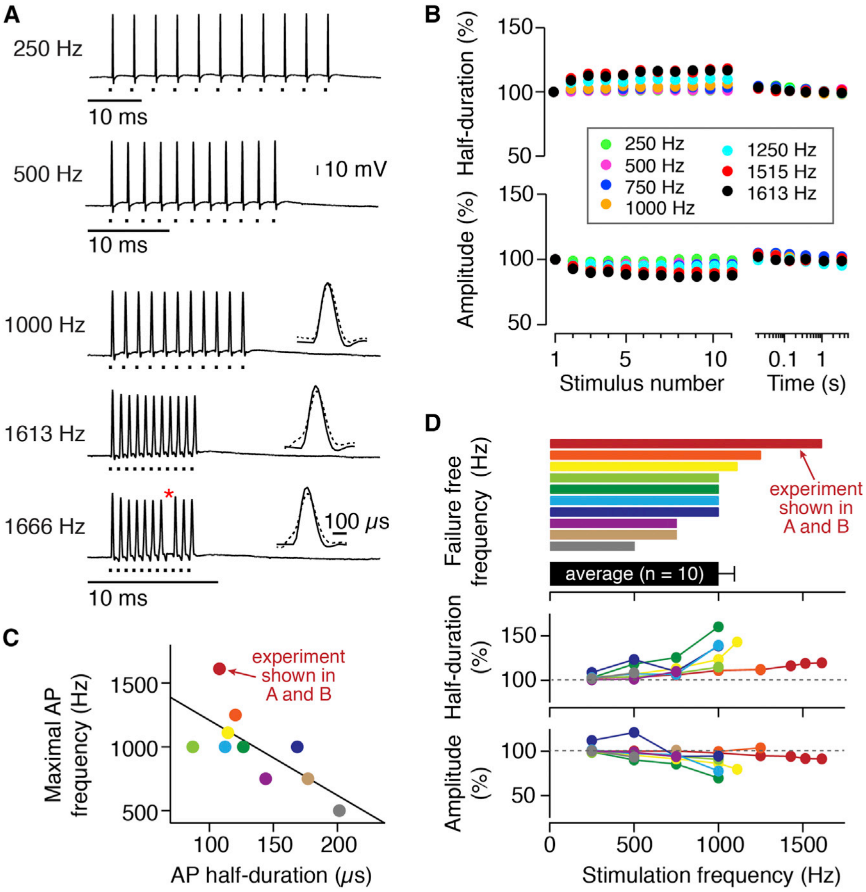

Figure 4. Stable APs during kHz Bursts

(A) Examples of APs recorded in a cMFB elicited at the indicated frequencies by axonal stimulation with an extracellular stimulation pipette (stimulation time points are indicated as dots below the traces; lowest scale bar applies to all three lowest traces). An overlay of the first (solid) and last (11th, dashed) AP is shown on the right. Note the failure after the seventh AP at 1,666 Hz (red asterisk).

(B) Time course of AP broadening and amplitude reduction of the experiment shown in (A) at the color-coded frequencies. The amplitude and half-duration of 11 APs during the train are plotted versus the stimulus number (normalized to the first AP). The properties of the APs that were elicited with increasing intervals following the train stimulation (not shown in A) are plotted versus the time after the end of the train. Note the stable half-duration and amplitude during bursts of up to 1 kHz frequency.

(C) Correlation of the maximal failure-free AP frequency and the AP half-duration recorded in n = 10 mossy fibers (Pearson's correlation coefficient R = −0.71; p = 0.02).

(D) Maximum failure-free frequency plotted versus stimulation frequency (top). The black bar shows the mean ± SEM (n = 10); colors indicate individual experiments. Corresponding half-duration (middle) and amplitude (bottom) of the last AP in the train normalized to the first AP.

(Figure 7B). Whereas capacitance measurements sample the total release from the entire cMFB, deconvolution based on the postsynaptic current from a GC samples only the fraction of total release of the cMFB that is directed toward the single GC recorded from (see illustration in Figure 7A). Therefore, quantitative comparison of the number of released vesicles with both techniques results in an estimate of the number of postsynaptic GCs per cMFB for each cMFB-GC pair. Assuming a single vesicle capacitance of 70 aF, the comparison revealed on average 100 ± 10 GCs per cMFB (Figure 7C, n = 10 cell pairs). This is higher than previous estimates (~10, Billings et al., 2014; ~50, Jakab and Hámori, 1988), but, e.g., a bias towards larger terminals, ectopic vesicle release, postsynaptic rundown, or release onto Golgi cells would lead to an overestimation of the connectivity ratio. Thus, we established two independent techniques with high temporal resolution, which allowed us to measure release at cMFBs directly.

Ultrafast Vesicle Recruitment and Tight Ca^{2+} Channel-Vesicle Coupling

Next we determined the number of release-ready vesicles, a central parameter to understanding the mechanisms of high-frequency synaptic transmission (Hallermann and Silver, 2013; Neher, 2010). The release rate based on deconvolution techniques showed an initial peak and a subsequent sustained part (cf. Figure 7A). The first peak most likely reflects fusion of release-ready vesicles, whereas the sustained part reflects vesicle recruitment (Sakaba and Neher, 2001b). Analysis of the cumulative release rates (Figure 8A) revealed that the initial release was best described by two exponential components with time constants of 0.43 ± 0.05 and 5.6 ± 1.4 ms (consisting of N_1 = 15.2 ± 4.3 and N_2 = 7.3 ± 1.4 vesicles; n = 10; Table S1). These estimates of the number of release-ready vesicles are slightly higher than estimates using extracellular stimulation techniques (5–10 vesicles; Saviane and Silver, 2006; Hallermann et al., 2010), but much smaller than estimates at the calyx of Held (range 700–5,000; Borst and Soria van Hoeve, 2012). The sustained part was well described by a line with an average slope of 358 ± 132 vesicles $\cdot$ s^{-1} (n = 10; Figure 8A; Table S1). These data indicate two populations of release-ready vesicles and a rapid recruitment speed of ~350 vesicles $\cdot$ s^{-1}, which can be sustained for up to 100 ms.

To analyze the coupling distance of vesicles to Ca^{2+} channels, we substantially increased the intrabouton Ca^{2+} buffering by raising the concentration of the slow Ca^{2+} buffer EGTA in the presynaptic solution from our control value of 200 μM to 5 mM. The time constant and the amplitude of the first component of release were not significantly changed by 5 mM EGTA (p = 0.42 and 0.96, respectively, Mann-Whitney U test; Figure 8A), which indicates that these vesicles are tightly coupled to Ca^{2+} channels. However, including 5 mM EGTA in the presynaptic pipette resulted in a decrease of the slowly releasing

Please cite this article in press as: Ritzau-Jost et al., Ultrafast Action Potentials Mediate Kilohertz Signaling at a Central Synapse, Neuron (2014), http://dx.doi.org/10.1016/j.neuron.2014.08.036

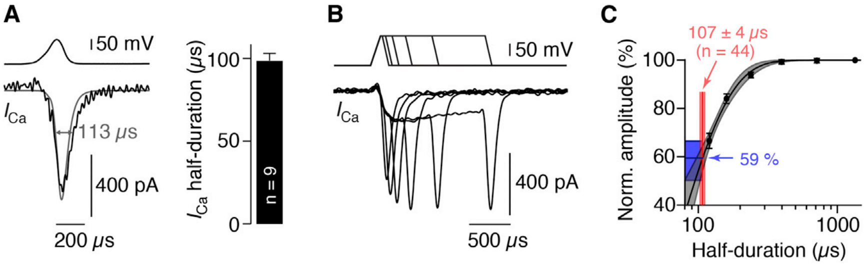

Figure 5. Efficient Opening of Ca^{2+} Channels during cMFB APs

(A) Left: Pharmacologically isolated Ca^{2+} current (I_{Ca}, bottom) evoked by an AP voltage command recorded in a cMFB (top) superimposed with the prediction of a m^2 Hodgkin-Huxley model calculated with the AP-voltage command. The half-duration of the measured current is indicated. Right: Average half-duration of the measured Ca^{2+} current (mean ± SEM; n represents number of cMFBs).

(B) Pharmacologically isolated Ca^{2+} current evoked by AP-like voltage commands of different half-durations (120, 160, 240, 400, 720, 1,360 μs).

(C) Peak amplitudes of Ca^{2+} currents evoked by AP-like voltage commands. Data (means ± SEM, n = 10) were normalized to the maximum value of each experiment and fit with a monoexponential function (black line). Superposition of the 95% confidence band of the fit (gray) with the average AP half-duration (104 ± 7 μs, n = 44; red) results in an estimate of relative Ca^{2+} channel open probability during an AP of 59% with a range of 50%–66% (blue; see also Figure S4).

component (N_2, $p < 0.01$, Mann-Whitney U test; Figure 8A), suggesting that these vesicles are remote from Ca^{2+} channels (Wadel et al., 2007) or that they have a lower intrinsic Ca^{2+} affinity (Lee et al., 2013; Wölfel et al., 2007). The slope of the linear part of the fits was not reduced with 5 mM EGTA (p = 0.11, Mann-Whitney U test; Figure 8A), indicating that EGTA does not block recruitment of vesicles to the release site. We further analyzed the kinetics of release with capacitance measurements. As with deconvolution techniques, two components of release and a linear vesicle recruitment rate were observed. The second release component was blocked by 5 mM EGTA, but the slope of the linear component was unaffected (Figure 8B; Table S1).

To relate these parameters to release evoked by AP trains, we recorded EPSCs in GCs elicited by extracellular stimulation of mossy fibers at 300 Hz (Figure 8C). We analyzed the number of release-ready vesicles and the vesicle recruitment rate by back-extrapolation of the cumulative EPSC amplitude (Figure 8D; Schneggenburger et al., 1999; Thanawala and Regehr, 2013). This analysis revealed 13.7 ± 3.4 release-ready vesicles and a recruitment rate of 469 ± 150 s^{-1} (n = 10), consistent with previous estimates at this synapse (Saviane and Silver, 2006; Hallermann et al., 2010). Interestingly, the values are similar to N_1 and s determined with prolonged depolarizations (cf. Figure 8A). This indicates that fast-releasing (N_1) but not slow-releasing vesicles (N_2) contribute to AP-evoked release (Sakaba, 2006) and that the maximal vesicle recruitment rate is similar during AP trains and prolonged presynaptic voltage steps. Furthermore, application of the membrane-permeable Ca^{2+} chelator EGTA-AM (100 μM) reduced the EPSC amplitude by 37% ($p < 0.01$, Wilcoxon signed-rank test; Figure 8C). Since 100 μM EGTA-AM was continuously applied at physiological temperatures, the intracellular EGTA concentration could be much higher than 5 mM. Therefore, no conclusions about the coupling distance can be drawn from these experiments. In contrast, the rate of vesicle recruitment was not significantly changed upon EGTA-AM application (p = 0.77, Wilcoxon signed-rank test; Figure 8D), which is again consistent with the lack of effect of 5 mM EGTA on the vesicle recruitment rate during depolarizations (cf. Figure 8A). In order to relate the recruitment rate to the vesicles that contribute to AP-evoked release, we divided the recruitment rate by the number of fast-releasing vesicles that mediate AP-evoked release. This resulted in a recruitment rate of 24 s^{-1} with prolonged depolarization using deconvolution, 50 s^{-1} with prolonged depolarization using capacitance measurements, and 34 s^{-1} with train stimulation using back-extrapolation (Table S1). Thus, deconvolution technique, capacitance measurements, and train stimulation revealed a small pool of release-ready vesicles, containing vesicles tightly coupled to Ca^{2+} channels, and rapid vesicle recruitment that can be sustained for > 100 ms.

DISCUSSION

In this study, paired recordings between cMFBs and GC allowed us to analyze the mechanisms of high-frequency signaling at highly divergent presynaptic boutons transmitting onto dozens of postsynaptic partners (Jörntell and Ekerot, 2006; Rancz et al., 2007; Saviane and Silver, 2006). We identified a unique set of presynaptic properties enabling single cMFB-GC connections to sustain kHz transmission during short bursts of APs: ultrafast, metabolically efficient APs can occur at bursts of up to 1.5 kHz, $Ca_v2.1$ Ca^{2+} channels open efficiently during APs, a subset of vesicles is tightly coupled to Ca^{2+} channels, and vesicles are rapidly recruited to the release site. Thus, our results establish a set of parameters enabling central synapses to operate in the kHz range.

Ultrafast APs

The AP is the basal unit for neuronal information processing, and its duration represents an ultimate limit for the maximal firing frequency. We recorded APs in cMFBs with ~100 μs half-duration (Figure 2). All previously measured AP half-durations are at least 2-fold longer. This is surprising because the AP shape has been studied extensively at a large number of cell types, including cells that transmit high-frequency signals (Borst and Sakmann, 1998; Rancz et al., 2007; Sabatini and Regehr, 1996). At cMFBs, previous estimates of AP half-duration in rats at physiological temperature (Rancz et al., 2007) and in turtles at room temperature (Thomsen et al., 2010) were several-fold longer; however, species differences and different recording conditions may account for this discrepancy. Yet extracellular recordings from cats in vivo are consistent with 100 μs half-durations of APs in cMFBs (Garwicz et al., 1998). Furthermore, a half-duration of ~100 μs is expected for the mature calyx of Held at physiological

Please cite this article in press as: Ritzau-Jost et al., Ultrafast Action Potentials Mediate Kilohertz Signaling at a Central Synapse, Neuron (2014), http://dx.doi.org/10.1016/j.neuron.2014.08.036

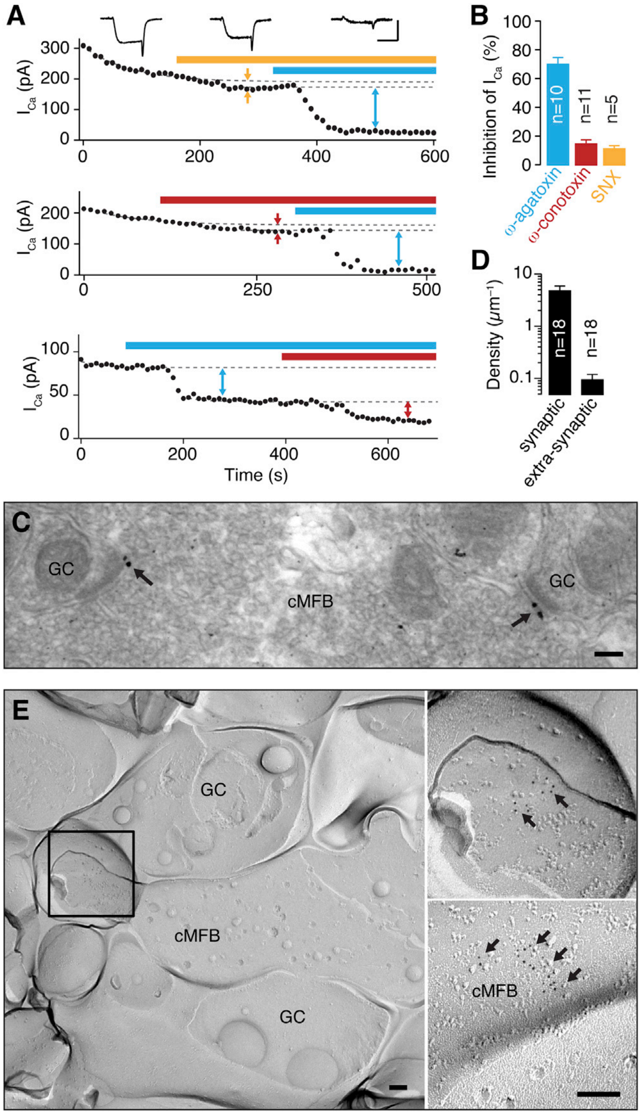

Figure 6. Ca$_v$2.1 Ca^{2+} Channels at Active Zones of cMFBs

(A) Steady-state amplitude of Ca^{2+} currents evoked by 3 ms depolarizations to 0 mV before and during application of 0.5 µM SNX-482 and 0.5 µM ω-Agatoxin (top), 1 µM ω-Conotoxin and 0.5 µM ω-Agatoxin (middle), or 0.5 µM ω-Agatoxin and 1 µM ω-Conotoxin (bottom). Horizontal bars indicate time of toxin application and dashed lines represent single exponential fits to the initial part of Ca^{2+} current amplitudes to account for rundown. Inset: Example Ca^{2+} currents for the first shown experiment before (left trace) and after wash-in of the toxins (middle and right traces). Scale bars, 200 pA and 2 ms.

(B) Average inhibition of Ca^{2+} currents by 0.5 µM ω-Agatoxin, 1 µM ω-Conotoxin, and 0.5 µM SNX-482 (mean ± SEM).

(C) Pre-embedding immunogold electron-microscopic labeling showing localization of Ca$_v$2.1 Ca^{2+} channels in the presynaptic active zones of a cMFB from a wild-type mouse. GC, granule cell dendrite. Arrows point toward gold particles. Scale bar, 100 nm.

(D) Average Ca$_v$2.1 immunogold density in cMFB profiles within and outside the active zones on a logarithmic scale (mean ± SEM).

(E) Freeze-fracture replica electron micrograph showing clusters of Ca$_v$2.1 Ca^{2+} channels in cMFBs from a 3-week-old mouse. Left: Low-magnification electron micrograph showing cross-fracture of a mossy fiber terminal (cMFB) with vesicles and continuous P-face of the same terminal contacting a granule cell dendrite (GC). A square part is enlarged (upper right) to show nine particles for Ca$_v$2.1 clustered at the active zone. Lower right: The picture derives from a different cMFB showing 17 particles. Arrows point toward gold particles. Scale bars, 100 nm.

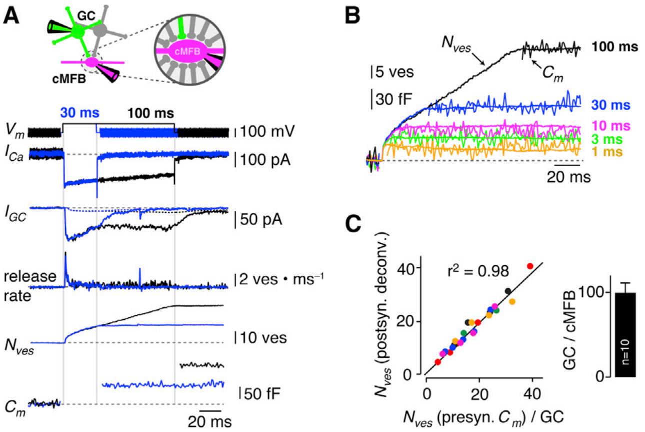

Figure 7. Measuring Vesicular Release Simultaneously from Presynaptic Capacitance Increase and Postsynaptic Currents

(A) Top: Illustration of the paired cMFB-GC recording configuration. The inset highlights the divergence of each cMFB contacting the GC recorded from (green) as well as many other GCs' dendrites (gray). Below: Example voltage command for cMFB (V_m), Ca^{2+} current in cMFB (I_{Ca}), EPSC in the GC (I_{GC}), deconvolved release rate, cumulative release rate (N_{ves}), and the capacitance increase in the cMFB (C_m) are plotted for a 30 ms (blue) and 100 ms (black) cMFB depolarization.

(B) Superposition of capacitance increase (C_m) in cMFB and cumulative release rate (N_{ves}) estimated by deconvolution of the postsynaptic GC EPSC for different pulse durations as indicated for the example experiment shown in (A).

(C) Left: Comparison of the presynaptic (C_m) and postsynaptic (deconvolution) estimates of the number of released vesicles per MF-GC connection. Each color represents a paired cMFB-GC recording with duration of depolarizations ranging from 1 to 100 ms. Right: Resulting average number of GC per cMFB based on n = 10 paired recordings (mean ± SEM).

temperature (Taschenberger and von Gersdorff, 2000), although such recordings have not been performed, and previously measured values at the immature calyx or at room temperatures were > 200 µs (Borst and Sakmann, 1998; Taschenberger and von Gersdorff, 2000; Yang and Wang, 2006). In general, fast-spiking neurons seem to have APs with short duration (Carter and Bean, 2009). Accordingly, maximal firing frequency and AP half-duration were correlated within the here-analyzed population of cMFBs (Figure 4C). Similar results have been obtained at two classes of vestibular nucleus neurons (Gittis et al., 2010). The very short half-duration of APs in cMFBs likely represents a special adaptation to the high frequencies that these presynaptic terminals operate at (Figure 4; Rancz et al., 2007).

To get an insight into the underlying mechanisms, we analyzed the properties of Na$^+$ and K$^+$ channels. Our estimated Na$^+$ current density was similar to the density at axons of hippocampal interneurons (Hu and Jonas, 2014). Furthermore, Na$^+$ channels were rapidly inactivating, resulting in a Na$^+$ excess ratio of ~1.8 (Figure 3), which is similar to the axon initial segment of layer 5 pyramidal cells (Hallermann et al., 2012) and slightly larger

Please cite this article in press as: Ritzau-Jost et al., Ultrafast Action Potentials Mediate Kilohertz Signaling at a Central Synapse, Neuron (2014), http://dx.doi.org/10.1016/j.neuron.2014.08.036

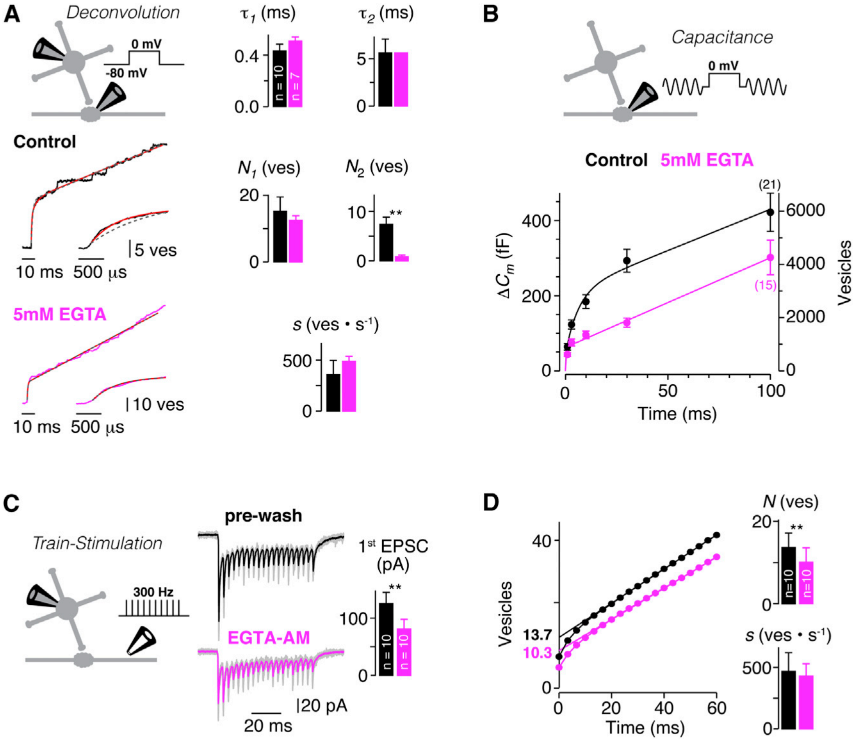

Figure 8. Ultrafast Vesicle Recruitment and Tight Ca^{2+} Channel-Vesicle Coupling

(A) Left: Example of cumulative release rates during a 100 ms depolarization in control (black; presynaptic pipette contained 200 µM EGTA) and with increased Ca^{2+} buffering in the cMFB (magenta; 5 mM EGTA) superimposed with a fit consisting of the sum of a biexponential function and a line (red) and the sum of a monoexponential function and a line (dashed gray). Inset: Initial cumulative release rate on an expanded timescale. Right: Average fit parameters of the sum of a biexponential function and a line for control (black) and high-EGTA conditions (magenta; mean ± SEM; n represents the number of paired cMFB-GC recordings). For 5 mM EGTA, τ_2 was fixed to the control value.

(B) Average capacitance increases (ΔC_m) plotted versus the length of the depolarizing pulse in control condition (black; n = 21) and with 5 mM EGTA (magenta; mean ± SEM; n = 15; n represents the number of cMFB recordings). The right axis indicates the number of vesicles based on 70 aF/vesicle. See Table S1 for parameters of the fits.

(C) Left: Example EPSCs (gray) evoked by 300 Hz axonal stimulation (20 stimuli; recording configuration depicted by the inset) recorded in a cMFB superimposed with the corresponding average before (black) and after bath application of 100 µM EGTA-AM (magenta). Right: Average amplitude of the first EPSC for control and EGTA-AM (black and magenta, respectively; mean ± SEM; n = 10).

(D) Left: Average cumulative number of released vesicles before (black) and after application of EGTA-AM (magenta). The estimated number of release-ready vesicles by back-extrapolation is indicated. Right: Average number of release-ready vesicles (*N*) and slope (*s*) estimated from the back-extrapolation of individual experiments before and after application of EGTA-AM (mean ± SEM; see also Table S1).

than at hippocampal mossy fiber boutons (Alle et al., 2009). The AP efficiency is surprising because short half-durations of APs tend to come at a cost of metabolic inefficiency (Carter and Bean, 2009, 2011).

The repolarization of cMFB APs was mediated by both K_{v1} and K_{v3} channels (Figure 2). This is in contrast to findings at the Purkinje cell soma, the boutons of cerebellar interneuron axons, or the calyx of Held, where K_{v3} dominates the repolarization (Ishikawa et al., 2003; Martina et al., 2007; Rowan et al., 2014; Wang et al., 1998). However, both K_{v1} and K_{v3} channels cause the repolarization of hippocampal mossy fiber boutons (Alle et al., 2011). The speed of K^+ channel activation measured here at cMFBs was fast, but comparable to K^+ channel activation kinetics measured previously (Alle et al., 2011; Martina et al., 2007), indicating that the ultrafast APs at cMFBs cannot be explained by rapid activation kinetics alone. Indeed, our Hodgkin-Huxley modeling based on measured gating kinetics predicted a high density of K^+ channels at cMFBs (Figure S3). However, in most outside-out patches from cMFBs, the estimated K^+ current density was low. This discrepancy is consistent with electron microscopic analysis showing that K_{v1} channels are highly clustered at fine protuberances of cMFBs, making density estimates from outside-out patches unreliable (Figure S3E; McNamara et al., 1996). In addition, cMFBs and the adjacent myelinated axons have structural similarities with nodes of Ranvier (Palay and Chan-Palay, 1974), suggesting that K^+ channels are clustered at the adjacent mossy fiber axon comparable to the K^+ channel clustering observed at juxtaparanodal zones of the nodes of Ranvier (Rasband and Shrager, 2000). Thus, although we have no direct experimental evidence, our results suggest a high density of inhomogeneously distributed K^+ channels. Furthermore, our data indicate a high density of rapidly gating Na^+ channels underlying ultrafast but metabolically efficient APs at cMFBs.

Presynaptic Ca^{2+} Currents

The exceptionally short duration of cMFB APs raised the question how Ca^{2+} channels are recruited during APs. In principle, reliable synaptic transmission can be obtained either by efficient opening of few presynaptic Ca^{2+} channels during APs (as shown, e.g., at the calyx of Held; Borst and Sakmann, 1998; but see also Sheng et al., 2012) or by inefficient opening of many Ca^{2+} channels (as shown, e.g., at the neuromuscular junction; Luo et al., 2011). Our analysis indicates efficient Ca^{2+} channel opening despite the short duration of APs (Figure 5). This implies that activation kinetics of Ca^{2+} channels is very fast. Indeed, experiments with step-like depolarizations revealed activation kinetics of < 100 µs at 0 mV (Figure S4). This is more than 5-fold faster than previous estimates at central synapses at room temperature (Borst and Sakmann, 1998; Li et al., 2007; Lin et al., 2011) and is consistent with a strong temperature dependence of Ca^{2+} channel kinetics (Sabatini and Regehr, 1996). Furthermore, a Hodgkin-Huxley-type model of Ca^{2+} channels based on the measured activation and inactivation kinetics predicted efficient

Please cite this article in press as: Ritzau-Jost et al., Ultrafast Action Potentials Mediate Kilohertz Signaling at a Central Synapse, Neuron (2014), http://dx.doi.org/10.1016/j.neuron.2014.08.036

channel opening. To gain insight into the molecular mechanism of fast Ca^{2+} channel gating, we determined the contribution of the different Ca^{2+} channel subtypes at cMFBs. Electrophysiological recordings showed that $Ca_v2.1$ Ca^{2+} channels contribute ~70% of the total Ca^{2+} current in cMFBs (Figure 6B). Furthermore, pre-embedding immunogold and freeze-fracture replica labeling indicated clustering of $Ca_v2.1$ Ca^{2+} channels at the active zone (Figures 6C and 6D). Thus, rapidly activating $Ca_v2.1$ Ca^{2+} channels ensure efficient calcium influx at the active zone during fast cMFB APs.

Tight Vesicle to Ca^{2+} Channel Coupling

The first component of release was not significantly slowed by 5 mM EGTA in cMFB (Figure 8A). In contrast, at the immature calyx of Held synapse, 5 mM EGTA prolonged the first component of release (Sakaba and Neher, 2001a). Thus, compared with loose vesicle to Ca^{2+} channel coupling at the immature calyx (Meinrenken et al., 2002), the mature cMFBs studied here display tight vesicle to Ca^{2+} channel coupling. Tight coupling has been observed at many synapses mediating high frequency synaptic transmission, such as the mature calyx of Held (Wang et al., 2008), the hippocampal basket cell to granule cell synapse (Bucurenciu et al., 2008), and the parallel fiber to Purkinje cell synapse (Schmidt et al., 2013). On the other hand, the mature hippocampal mossy fiber to CA3 pyramidal cell synapse exhibits loose coupling (Vyleta and Jonas, 2014). The tight and loose vesicle to Ca^{2+} channel coupling in cerebellar and hippocampal mossy fiber boutons, respectively, seems consistent with their markedly different function within the corresponding neuronal network (Delvendahl et al., 2013).

Vesicle Recruitment Rate

We found a vesicle recruitment rate of ~400 vesicles • s^{-1} during 100 ms depolarizations and during high-frequency synaptic transmission for each cMFB-GC connection at physiological temperatures (Figure 8). For the entire cMFB, the rate was 30,000 vesicles • s^{-1} (Figure 8B). At the calyx of Held synapse, at which vesicle recruitment has been intensely studied, a value of less than 10,000 vesicles • s^{-1} has been estimated at room temperature (Neher, 2010; Sakaba and Neher, 2001b; Wölfel et al., 2007), but higher values have also been obtained (100,000 and 170,000 vesicles • s^{-1}, at room and physiological temperatures; based on 7,500 and 12,300 fF/s, respectively; Kushmerick et al., 2006). Relating the vesicle recruitment rate to the number of fast-releasing vesicles in cMFBs resulted in estimates ranging from 24 to 50 s^{-1} (Figure 8). This is lower than previous estimates based on postsynaptic techniques at cMFBs (~70 s^{-1}; Saviane and Silver, 2006; Hallermann et al., 2010), but higher than estimates at the calyx of Held (~11 s^{-1}; physiological temperature; Kushmerick et al., 2006). High rates of vesicle recruitment have also been observed at cerebellar parallel fibers (Crowley et al., 2007; Valera et al., 2012; but see van Beugen et al., 2013). Thus, vesicle recruitment at cMFBs is remarkably fast.

Limited Surface Area at a Highly Divergent Synapse

One obvious explanation for the high vesicle recruitment rate in cMFBs could reside in the fact that each cMFB contacts more than 10 dendrites of GCs (Billings et al., 2014; Jakab and Hámori, 1988; Figure 7C). This limits the surface area that is available for each postsynaptic partner. The limited number of release sites must therefore rely on rapid vesicle recruitment (Saviane and Silver, 2006). Consistently, the cMFB-GC synapse has been described as a “device to secure a high mossy fiber to GC divergence with minimal physical structure” (Eccles et al., 1967). In contrast, large synapses with 1:1 connectivity, such as the neuromuscular junction (Luo et al., 2011), the Purkinje cell to cerebellar nuclear neuron synapse (Telgkamp et al., 2004), the hippocampal mossy fiber to CA3 pyramidal neuron synapse (Hallermann et al., 2003), the vestibular afferent synapse (Bagnall et al., 2008), and the endbulb of Held synapse (Lin et al., 2011), rely on a large pool of release-ready vesicles with low release probabilities. Therefore, these 1:1 synapses can sustain efficient release by the parallel usage of many release sites despite slow vesicle recruitment at each site, whereas cMFB-GC synapses sustain efficient release with fewer release sites and rapid vesicle recruitment (cf. Box 1 in Hallermann and Silver, 2013). Thus, the limited space for synaptic contact at the cMFB-GC synapse might provide an explanation for the rapid vesicle recruitment.

Implications for Information Processing

To control timing (Ivry and Keele, 1989), the cerebellar cortex relies on high-frequency firing of mossy fibers (Garwicz et al., 1998; Rancz et al., 2007), granule cells (Jörntell and Ekerot, 2006), and Purkinje cells (Blot and Barbour, 2014; Thach, 1972). Quantitative comparison of these data suggests that the frequency of a signal is highest in mossy fibers and gradually becomes lower during propagation through granule and Purkinje cells. Interestingly, GCs may linearly encode the strength of cMFB firing (Chadderton et al., 2004; Gabbiani et al., 1994). Linear processing also occurs at parallel fiber to Purkinje cell transmission, but in a lower frequency range (Walter and Khodakhah, 2006). The frequency reduction and the linear processing suggest that the cerebellar cortex receives mossy fiber input in the kHz range (Rancz et al., 2007; Figure 4), performs additive and (via gain modulation) multiplicative scaling of rate-coded inputs (Silver, 2010), and provides an output at frequencies still high but lower than the input. Thereby, computation at exceptionally fast timescales can be achieved. Future studies will have to analyze the advantages of high-frequency firing of individual neurons, in particular in consideration of the fact that other brain regions, such as the visual system, can process information rapidly, even though the firing rates of the individual neurons are much lower (Rieke et al., 1997; Tchumatchenko et al., 2011).

In summary, by using paired recordings between cMFBs and GCs in combination with high-resolution techniques, we were able to directly measure fundamental parameters that enable high-frequency synaptic transmission. Our study provides insight into the exceptionally diverse repertoire of synaptic functions at central synapses.

EXPERIMENTAL PROCEDURES

Methods are described in detail in the Supplemental Experimental Procedures.

Presynaptic Recordings from cMFBs

Recordings were performed in acute sagittal cerebellar slices from mature (>P20) TgN(Thy1-EYFP) (Hirrlinger et al., 2005) or C57BL/6 mice at 35°C – 37°C. To increase the success rate of presynaptic recordings from cMFBs, two-photon guided patch-clamp recordings (Margrie et al., 2003) were performed in the TgN(Thy1-EYFP)-mice with a Femto-2D two-photon microscope (Femtonics, Budapest) and a 60x Olympus (NA 1.0) objective. Alternatively, cMFBs were identified with infrared differential interference contrast (DIC) optics using a FN-1 microscope from Nikon with a 100x objective (NA 1.1). All current-clamp and voltage-clamp recordings from cMFBs and GCs were performed with an EPC10/2 amplifier (HEKA Elektronik, Lambrecht/Pfalz).

Identification of cMFB Recordings

To unequivocally identify cMFBs, two alternative methods were used: (1) in presynaptic recordings with potassium-based intracellular solutions, the distinctive electrical properties including pronounced outward rectification and time-dependent "sag" of membrane potential on hyperpolarization were used (Rancz et al., 2007); (2) in presynaptic recordings with cesium-based intracellular solutions (and TTX in the bath), the capacitance increase upon depolarization confirmed the identity of cMFBs, since other cells such as GCs did not show capacitance increases (if any, < 20 fF). In addition, Atto 594 in the presynaptic intracellular solution allowed visualizing the mossy fiber axon.

Paired Recordings between cMFBs and GC

For paired pre- and postsynaptic recordings, GCs were whole-cell patch-clamped with intracellular solution containing 100 μM Atto 594 or Atto 488, and cMFBs near dendrites were identified by their EYFP expression in TgN(Thy1-EYFP) mice or by differential interference contrast microscopy. The reliable induction of an EPSC in the GC upon depolarization of the presynaptic structure was used to unequivocally identify a cMFB.

SUPPLEMENTAL INFORMATION

Supplemental Information includes Supplemental Experimental Procedures, four figures, and one table and can be found with this article online at http://dx.doi.org/10.1016/j.neuron.2014.08.036.

ACKNOWLEDGMENTS

We would like to thank Erwin Neher for helpful discussions and for advice during the implementation of the deconvolution of postsynaptic currents; Erwin Neher, Maarten Kole, and Manfred Heckmann for critically reading the manuscript; Masahiko Watanabe for providing Ca$_v$2.1 antibody; and Walter Kaufmann for technical assistance. This work was supported by the Heisenberg Program of the German Research Foundation to S.H. (HA 6386/1-1, 2-1, and 3-1) and by the German Research Foundation to J.H. (HI1414/2-1) and partly funded by the Wellcome Trust (ref: 097829) through the Centre for Chronic Diseases and Disorders (C2D2) at the University of York.

Accepted: August 17, 2014
Published: September 11, 2014

REFERENCES

Alle, H., Roth, A., and Geiger, J.R.P. (2009). Energy-efficient action potentials in hippocampal mossy fibers. Science *325*, 1405–1408.

Alle, H., Kubota, H., and Geiger, J.R. (2011). Sparse but highly efficient K$_v$3 outpace BK$_{Ca}$ channels in action potential repolarization at hippocampal mossy fiber boutons. J. Neurosci. *31*, 8001–8012.

Arenz, A., Silver, R.A., Schaefer, A.T., and Margrie, T.W. (2008). The contribution of single synapses to sensory representation in vivo. Science *321*, 977–980.

Bagnall, M.W., McElvain, L.E., Faulstich, M., and du Lac, S. (2008). Frequency-independent synaptic transmission supports a linear vestibular behavior. Neuron *60*, 343–352.

Bean, B.P. (2007). The action potential in mammalian central neurons. Nat. Rev. Neurosci. *8*, 451–465.

Billings, G., Piasini, E., Lőrincz, A., Nusser, Z., and Silver, R.A. (2014). Network structure within the cerebellar input layer enables lossless sparse encoding. Neuron *83*, 960–974.

Blot, A., and Barbour, B. (2014). Ultra-rapid axon-axon ephaptic inhibition of cerebellar Purkinje cells by the pinceau. Nat. Neurosci. *17*, 289–295.

Borst, J.G., and Sakmann, B. (1998). Calcium current during a single action potential in a large presynaptic terminal of the rat brainstem. J. Physiol. *506*, 143–157.

Borst, J.G., and Soria van Hoeve, J. (2012). The calyx of held synapse: from model synapse to auditory relay. Annu. Rev. Physiol. *74*, 199–224.

Bucurenciu, I., Kulik, A., Schwaller, B., Frotscher, M., and Jonas, P. (2008). Nanodomain coupling between Ca^{2+} channels and Ca^{2+} sensors promotes fast and efficient transmitter release at a cortical GABAergic synapse. Neuron *57*, 536–545.

Carter, B.C., and Bean, B.P. (2009). Sodium entry during action potentials of mammalian neurons: incomplete inactivation and reduced metabolic efficiency in fast-spiking neurons. Neuron *64*, 898–909.

Carter, B.C., and Bean, B.P. (2011). Incomplete inactivation and rapid recovery of voltage-dependent sodium channels during high-frequency firing in cerebellar Purkinje neurons. J. Neurophysiol. *105*, 860–871.

Chadderton, P., Margrie, T.W., and Häusser, M. (2004). Integration of quanta in cerebellar granule cells during sensory processing. Nature *428*, 856–860.

Crowley, J.J., Carter, A.G., and Regehr, W.G. (2007). Fast vesicle replenishment and rapid recovery from desensitization at a single synaptic release site. J. Neurosci. *27*, 5448–5460.

Delvendahl, I., Weyhersmüller, A., Ritzau-Jost, A., and Hallermann, S. (2013). Hippocampal and cerebellar mossy fibre boutons - same name, different function. J. Physiol. *591*, 3179–3188.

DiGregorio, D.A., Nusser, Z., and Silver, R.A. (2002). Spillover of glutamate onto synaptic AMPA receptors enhances fast transmission at a cerebellar synapse. Neuron *35*, 521–533.

Eccles, J.C., Ito, M., and Szentagothai, J. (1967). The Cerebellum as a Neuronal Machine. (Berlin: Springer-Verlag).

Gabbiani, F., Midtgaard, J., and Knöpfel, T. (1994). Synaptic integration in a model of cerebellar granule cells. J. Neurophysiol. *72*, 999–1009.

Garwicz, M., Jörntell, H., and Ekerot, C.F. (1998). Cutaneous receptive fields and topography of mossy fibres and climbing fibres projecting to cat cerebellar C3 zone. J. Physiol. *512*, 277–293.

Geiger, J.R.P., and Jonas, P. (2000). Dynamic control of presynaptic Ca^{2+} inflow by fast-inactivating K$^+$ channels in hippocampal mossy fiber boutons. Neuron *28*, 927–939.

Gittis, A.H., Moghadam, S.H., and du Lac, S. (2010). Mechanisms of sustained high firing rates in two classes of vestibular nucleus neurons: differential contributions of resurgent Na, Kv3, and BK currents. J. Neurophysiol. *104*, 1625–1634.

Gutman, G.A., Chandy, K.G., Grissmer, S., Lazdunski, M., McKinnon, D., Pardo, L.A., Robertson, G.A., Rudy, B., Sanguinetti, M.C., Stühmer, W., and Wang, X. (2005). International Union of Pharmacology. LIII. Nomenclature and molecular relationships of voltage-gated potassium channels. Pharmacol. Rev. *57*, 473–508.

Hallermann, S., and Silver, R.A. (2013). Sustaining rapid vesicular release at active zones: potential roles for vesicle tethering. Trends Neurosci. *36*, 185–194.

Hallermann, S., Pawlu, C., Jonas, P., and Heckmann, M. (2003). A large pool of releasable vesicles in a cortical glutamatergic synapse. Proc. Natl. Acad. Sci. USA *100*, 8975–8980.

Hallermann, S., Fejtova, A., Schmidt, H., Weyhersmüller, A., Silver, R.A., Gundelfinger, E.D., and Eilers, J. (2010). Bassoon speeds vesicle reloading at a central excitatory synapse. Neuron *68*, 710–723.

Please cite this article in press as: Ritzau-Jost et al., Ultrafast Action Potentials Mediate Kilohertz Signaling at a Central Synapse, Neuron (2014), http://dx.doi.org/10.1016/j.neuron.2014.08.036

Hallermann, S., de Kock, C.P., Stuart, G.J., and Kole, M.H. (2012). State and location dependence of action potential metabolic cost in cortical pyramidal neurons. Nat. Neurosci. *15*, 1007–1014.

Hirrlinger, P.G., Scheller, A., Braun, C., Quintela-Schneider, M., Fuss, B., Hirrlinger, J., and Kirchhoff, F. (2005). Expression of reef coral fluorescent proteins in the central nervous system of transgenic mice. Mol. Cell. Neurosci. *30*, 291–303.

Hu, H., and Jonas, P. (2014). A supercritical density of Na^+ channels ensures fast signaling in GABAergic interneuron axons. Nat. Neurosci. *17*, 686–693.

Indriati, D.W., Kamasawa, N., Matsui, K., Meredith, A.L., Watanabe, M., and Shigemoto, R. (2013). Quantitative localization of $Ca_v2.1$ (P/Q-type) voltage-dependent calcium channels in Purkinje cells: somatodendritic gradient and distinct somatic coclustering with calcium-activated potassium channels. J. Neurosci. *33*, 3668–3678.

Ishikawa, T., Nakamura, Y., Saitoh, N., Li, W.B., Iwasaki, S., and Takahashi, T. (2003). Distinct roles of Kv1 and Kv3 potassium channels at the calyx of Held presynaptic terminal. J. Neurosci. *23*, 10445–10453.

Ivry, R.B., and Keele, S.W. (1989). Timing functions of the cerebellum. J. Cogn. Neurosci. *1*, 136–152.

Jakab, R.L., and Hámori, J. (1988). Quantitative morphology and synaptology of cerebellar glomeruli in the rat. Anat. Embryol. (Berl.) *179*, 81–88.

Jörntell, H., and Ekerot, C.F. (2006). Properties of somatosensory synaptic integration in cerebellar granule cells *in vivo*. J. Neurosci. *26*, 11786–11797.

Kushmerick, C., Renden, R., and von Gersdorff, H. (2006). Physiological temperatures reduce the rate of vesicle pool depletion and short-term depression via an acceleration of vesicle recruitment. J. Neurosci. *26*, 1366–1377.

Leão, R.M., Kushmerick, C., Pinaud, R., Renden, R., Li, G.L., Taschenberger, H., Spirou, G., Levinson, S.R., and von Gersdorff, H. (2005). Presynaptic Na^+ channels: locus, development, and recovery from inactivation at a high-fidelity synapse. J. Neurosci. *25*, 3724–3738.

Lee, J.S., Ho, W.K., Neher, E., and Lee, S.H. (2013). Superpriming of synaptic vesicles after their recruitment to the readily releasable pool. Proc. Natl. Acad. Sci. USA *110*, 15079–15084.

Li, L., Bischofberger, J., and Jonas, P. (2007). Differential gating and recruitment of P/Q-, N-, and R-type Ca^{2+} channels in hippocampal mossy fiber boutons. J. Neurosci. *27*, 13420–13429.

Lien, C.C., and Jonas, P. (2003). Kv3 potassium conductance is necessary and kinetically optimized for high-frequency action potential generation in hippocampal interneurons. J. Neurosci. *23*, 2058–2068.

Lin, K.H., Oleskevich, S., and Taschenberger, H. (2011). Presynaptic Ca^{2+} influx and vesicle exocytosis at the mouse endbulb of Held: a comparison of two auditory nerve terminals. J. Physiol. *589*, 4301–4320.

Liu, P.W., and Bean, B.P. (2014). Kv2 channel regulation of action potential repolarization and firing patterns in superior cervical ganglion neurons and hippocampal CA1 pyramidal neurons. J. Neurosci. *34*, 4991–5002.

London, M., Roth, A., Beeren, L., Häusser, M., and Latham, P.E. (2010). Sensitivity to perturbations *in vivo* implies high noise and suggests rate coding in cortex. Nature *466*, 123–127.

Luo, F., Dittrich, M., Stiles, J.R., and Meriney, S.D. (2011). Single-pixel optical fluctuation analysis of calcium channel function in active zones of motor nerve terminals. J. Neurosci. *31*, 11268–11281.

Margrie, T.W., Meyer, A.H., Caputi, A., Monyer, H., Hasan, M.T., Schaefer, A.T., Denk, W., and Brecht, M. (2003). Targeted whole-cell recordings in the mammalian brain in vivo. Neuron *39*, 911–918.

Martina, M., Metz, A.E., and Bean, B.P. (2007). Voltage-dependent potassium currents during fast spikes of rat cerebellar Purkinje neurons: inhibition by BDS-I toxin. J. Neurophysiol. *97*, 563–571.

McNamara, N.M., Averill, S., Wilkin, G.P., Dolly, J.O., and Priestley, J.V. (1996). Ultrastructural localization of a voltage-gated K^+ channel α subunit (K_V 1.2) in the rat cerebellum. Eur. J. Neurosci. *8*, 688–699.

Meinrenken, C.J., Borst, J.G., and Sakmann, B. (2002). Calcium secretion coupling at calyx of held governed by nonuniform channel-vesicle topography. J. Neurosci. *22*, 1648–1667.

Neher, E. (2010). What is rate-limiting during sustained synaptic activity: vesicle supply or the availability of release sites. Front Synaptic Neurosci *2*, 144, http://dx.doi.org/10.3389/fnsyn.2010.00144.

Palay, S.M., and Chan-Palay, V. (1974). Cerebellar Cortex: Cytology and Organization. (Berlin: Springer).

Rancz, E.A., Ishikawa, T., Duguid, I., Chadderton, P., Mahon, S., and Häusser, M. (2007). High-fidelity transmission of sensory information by single cerebellar mossy fibre boutons. Nature *450*, 1245–1248.

Rasband, M.N., and Shrager, P. (2000). Ion channel sequestration in central nervous system axons. J. Physiol. *525*, 63–73.

Rieke, F., Warland, D., de Ruyter van Steveninck, R.R., and Bialek, W. (1997). Spikes: Exploring the Neural Code. (Cambridge, Massachusetts: MIT Press).

Rowan, M.J.M., Tranquil, E., and Christie, J.M. (2014). Distinct K_v channel subtypes contribute to differences in spike signaling properties in the axon initial segment and presynaptic boutons of cerebellar interneurons. J. Neurosci. *34*, 6611–6623.

Rudy, B., and McBain, C.J. (2001). Kv3 channels: voltage-gated K^+ channels designed for high-frequency repetitive firing. Trends Neurosci. *24*, 517–526.

Sabatini, B.L., and Regehr, W.G. (1996). Timing of neurotransmission at fast synapses in the mammalian brain. Nature *384*, 170–172.

Sakaba, T. (2006). Roles of the fast-releasing and the slowly releasing vesicles in synaptic transmission at the calyx of held. J. Neurosci. *26*, 5863–5871.

Sakaba, T., and Neher, E. (2001a). Calmodulin mediates rapid recruitment of fast-releasing synaptic vesicles at a calyx-type synapse. Neuron *32*, 1119–1131.

Sakaba, T., and Neher, E. (2001b). Quantitative relationship between transmitter release and calcium current at the calyx of held synapse. J. Neurosci. *21*, 462–476.

Saviane, C., and Silver, R.A. (2006). Fast vesicle reloading and a large pool sustain high bandwidth transmission at a central synapse. Nature *439*, 983–987.

Schmidt, H., Brachtendorf, S., Arendt, O., Hallermann, S., Ishiyama, S., Bornschein, G., Gall, D., Schiffmann, S.N., Heckmann, M., and Eilers, J. (2013). Nanodomain coupling at an excitatory cortical synapse. Curr. Biol. *23*, 244–249.

Schneggenburger, R., Meyer, A.C., and Neher, E. (1999). Released fraction and total size of a pool of immediately available transmitter quanta at a calyx synapse. Neuron *23*, 399–409.

Sheng, M., Tsaur, M.L., Jan, Y.N., and Jan, L.Y. (1992). Subcellular segregation of two A-type K^+ channel proteins in rat central neurons. Neuron *9*, 271–284.

Sheng, J., He, L., Zheng, H., Xue, L., Luo, F., Shin, W., Sun, T., Kuner, T., Yue, D.T., and Wu, L.G. (2012). Calcium-channel number critically influences synaptic strength and plasticity at the active zone. Nat. Neurosci. *15*, 998–1006.

Silver, R.A. (2010). Neuronal arithmetic. Nat. Rev. Neurosci. *11*, 474–489.

Sun, J.Y., and Wu, L.G. (2001). Fast kinetics of exocytosis revealed by simultaneous measurements of presynaptic capacitance and postsynaptic currents at a central synapse. Neuron *30*, 171–182.

Taschenberger, H., and von Gersdorff, H. (2000). Fine-tuning an auditory synapse for speed and fidelity: developmental changes in presynaptic waveform, EPSC kinetics, and synaptic plasticity. J. Neurosci. *20*, 9162–9173.

Tchumatchenko, T., Malyshev, A., Wolf, F., and Volgushev, M. (2011). Ultrafast population encoding by cortical neurons. J. Neurosci. *31*, 12171–12179.

Telgkamp, P., Padgett, D.E., Ledoux, V.A., Woolley, C.S., and Raman, I.M. (2004). Maintenance of high-frequency transmission at purkinje to cerebellar nuclear synapses by spillover from boutons with multiple release sites. Neuron *41*, 113–126.

Thach, W.T. (1972). Cerebellar output: properties, synthesis and uses. Brain Res. *40*, 89–102.

Thanawala, M.S., and Regehr, W.G. (2013). Presynaptic calcium influx controls neurotransmitter release in part by regulating the effective size of the readily releasable pool. J. Neurosci. *33*, 4625–4633.

Thomsen, L.B., Jörntell, H., and Midtgaard, J. (2010). Presynaptic calcium signalling in cerebellar mossy fibres. Front Neural Circuits *4*, 1.

Valera, A.M., Doussau, F., Poulain, B., Barbour, B., and Isope, P. (2012). Adaptation of granule cell to Purkinje cell synapses to high-frequency transmission. J. Neurosci. *32*, 3267–3280.

van Beugen, B.J., Gao, Z., Boele, H.J., Hoebeek, F., and De Zeeuw, C.I. (2013). High frequency burst firing of granule cells ensures transmission at the parallel fiber to purkinje cell synapse at the cost of temporal coding. Front Neural Circuits *7*, 95.

von Gersdorff, H., Sakaba, T., Berglund, K., and Tachibana, M. (1998). Submillisecond kinetics of glutamate release from a sensory synapse. Neuron *21*, 1177–1188.

Vyleta, N.P., and Jonas, P. (2014). Loose coupling between Ca^{2+} channels and release sensors at a plastic hippocampal synapse. Science *343*, 665–670.

Wadel, K., Neher, E., and Sakaba, T. (2007). The coupling between synaptic vesicles and Ca^{2+} channels determines fast neurotransmitter release. Neuron *53*, 563–575.

Walter, J.T., and Khodakhah, K. (2006). The linear computational algorithm of cerebellar Purkinje cells. J. Neurosci. *26*, 12861–12872.

Wang, L.Y., and Kaczmarek, L.K. (1998). High-frequency firing helps replenish the readily releasable pool of synaptic vesicles. Nature *394*, 384–388.

Wang, L.Y., Gan, L., Forsythe, I.D., and Kaczmarek, L.K. (1998). Contribution of the Kv3.1 potassium channel to high-frequency firing in mouse auditory neurones. J. Physiol. *509*, 183–194.

Wang, L.Y., Neher, E., and Taschenberger, H. (2008). Synaptic vesicles in mature calyx of Held synapses sense higher nanodomain calcium concentrations during action potential-evoked glutamate release. J. Neurosci. *28*, 14450–14458.

Wölfel, M., Lou, X., and Schneggenburger, R. (2007). A mechanism intrinsic to the vesicle fusion machinery determines fast and slow transmitter release at a large CNS synapse. J. Neurosci. *27*, 3198–3210.

Yang, Y.M., and Wang, L.Y. (2006). Amplitude and kinetics of action potential-evoked Ca^{2+} current and its efficacy in triggering transmitter release at the developing calyx of held synapse. J. Neurosci. *26*, 5698–5708.

5 Zusammenfassung

Dissertation zur Erlangung des akademischen Grades: Dr. med.

Mechanismen hochfrequenter synaptischer Übertragung an einer zentralen Synapse

eingereicht von:	Andreas Ritzau-Jost, geboren Ritzau
angefertigt am:	Carl-Ludwig-Institut für Physiologie Medizinische Fakultät der Universität Leipzig
betreut von:	Prof. Dr. med. Stefan Hallermann
Eingereicht im:	April 2015

Um die synaptische Übertragung besser verstehen zu können, sind direkte, elektrophysiologische Messungen von präsynaptischen Strukturen erforderlich. Diese sind wegen struktureller Limitationen der meisten Präsynapsen schwer durchzuführen und bislang nur an wenigen Synapsen etabliert. Die vorliegende Studie macht sich die anatomischen Gegebenheiten des Cerebellums zu Nutze, das mit den cerebellären Moosfaserboutons über prominente Präsynapsen verfügt. Mit der direkten Messung an Moosfaserboutons und der Etablierung der zeitgleichen Ableitung postsynaptischer Signale (sogenannter „Paarableitungen“) sind neue Einblicke in die Funktionsweise einer der schnellsten Synapsen des zentralen Nervensystems gelungen. (Abbildung 1A, B im Manuskript; alle folgenden Abbildungsangaben beziehen sich auf Abbildungen des Publikationsmanuskripts unter Punkt 4)

Kilohertz-Signale zwischen Moosfaser und Körnerzelle (Abb. 1)

Frühere Studien haben an der Moosfaser-Körnerzell-Synapse hochfrequente Signaltransmission nachgewiesen. Die Bandbreite der zur Verfügung stehenden

Frequenzen war bislang jedoch nicht ausreichend erforscht. Diese spielt für die Informationscodierung im Nervensystem eine entscheidende Rolle. Es sollte die maximale Frequenz untersucht werden, bei der die Signalübertragung an dieser Synapse ohne Informationsverlust gelingt. In Paarableitungen wurden Moosfaserboutons mit Frequenzen von bis zu einem Kilohertz stimuliert und die dadurch hervorgerufenen postsynaptischen Ströme registriert. Kilohertz-Signale wurden dabei zuverlässig von der Prä- auf die Postsynapse übertragen (Abbildung 1D), wobei insbesondere im physiologisch relevanten Bereich von wenigen Stimuli stabile postsynaptische Ströme hervorgerufen wurden. Die Ergebnisse legen damit den Schluss nahe, dass Nervenzellen schneller als bislang gezeigt Informationen übertragen.

Ultraschnelle Aktionspotenziale (Abb. 2 und 3)

Aktionspotenziale limitieren die Frequenz, mit der Informationen neuronal codiert werden können. Damit ist die Kinetik des Aktionspotenzials entscheidender Parameter einer schnellen Signalübertragung. Trotz intensiver Untersuchung der Aktionspotenzial-Kinetik an verschiedenen Synapsen ist die in dieser Studie gemessene halbmaximale Aktionspotenzialdauer mit ~100 µs zweifach schneller als alle bisher gemessenen (Abbildung 2B, C). Außerdem war die halbmaximale Aktionspotenzialdauer an dieser Synapse in anderen Studien *in vitro* und *in vivo* mit über 600 Millisekunden bedeutend länger. Die Beobachtung schneller Aktionspotenziale stimmt jedoch mit der Beobachtung schnellerer Aktionspotenziale in hochfrequent codierenden Neuronen überein. Unsere Untersuchung der am Aktionspotenzial beteiligten Ionenkanäle zeigte eine schnelle Inaktivierung von Natrium-, sowie eine schnelle Aktivierung von Kaliumkanälen (Abbildung 2D, E und 3D). Die beobachtete Kanalkinetik führt zu einer erstaunlichen metabolischen Effizienz (Abbildung 3C).

Stabile Aktionspotenziale bei Kilohertzübertragung (Abb. 4)

Die Form von Aktionspotenzialen ändert sich in Abhängigkeit ihrer Frequenz und im Verlauf längerer Stimulation. Die Aktionspotenzialveränderungen bei hochfrequenter Stimulation waren deshalb von Interesse (dargestellt in Abbildung 4). Einige Präsynapsen leiteten Aktionspotenziale mit Frequenzen von bis zu 1.6 kHz stabil weiter (Abbildung 4A), wobei selbst bei diesen Raten nur eine geringe

Veränderung der Aktionspotenzial-Form auftrat (Abbildung 4B). Es konnte außerdem einen Zusammenhang zwischen der Dauer der Aktionspotenziale und der von individuellen Boutons erreichten, maximalen Aktionspotenzial-Rate festgestellt werden. Boutons mit längeren Halbwertszeiten der Aktionspotenziale erreichten dabei geringere Frequenzen als solche mit schnelleren Aktionspotenzialen (Abbildung 4C). Im Durchschnitt und in Übereinstimmung mit Ergebnissen aus Paarableitungen lag die maximal erreichte Signal-Rate bei circa einem Kilohertz (Abbildung 4D).

Kurze Aktionspotenziale öffnen effizient präsynaptische Calciumkanäle (Abb. 5 und 6)

Aktionspotenziale öffnen an Präsynapsen Calciumkanäle und setzen dadurch Neurotransmitter frei. Dabei hängt die Größe des Calciumstroms essenziell von der Kinetik des Aktionspotenzials ab. Messungen mit zuvor aufgezeichneten Aktionspotenzialen als Kommandostimulus zeigten, dass diese Calciumströme mit einer Halbwertsbreite von ~100 µm hervorrufen und dabei ~60% der präsynaptischen Calciumkanäle rekrutieren (Abbildung 5A, C). Bei der Anwendung selektiver, pharmakologischer Hemmstoffe zeigte sich, dass ~70% des Calciumeinstroms durch Kanäle vom $Ca_v2.1$ (P/Q)-Typ vermittelt werden (Abbildung 6A, B). Elektronenmikroskopische Aufnahmen mit Goldpartikel-markierten Antikörpern gegen den P/Q-Kanaltyp bestätigten deren Anreicherung an Freisetzungsstellen für Neurotransmitter (Abbildung 6C-E).

Schnelle Transmitterfreisetzung und –nachladung (Abb. 7 und 8)

Hohe Signalfrequenzen setzen eine schnelle Vesikelfusion und Nachladung von zur Freisetzung bereitstehenden Vesikeln voraus. Paarableitungen erlaubten die Bestimmung der Geschwindigkeit der Transmitterfreisetzung und –nachladung mit Hilfe von zwei Methoden (Abbildung 7): durch Vesikelfusion entstehende Oberflächenvergrößerungen der Präsynapse können in Form von Veränderungen der elektrischen Kapazität gemessen werden. Darüber hinaus kann die Transmitterfreisetzung aus den gleichzeitig aufgezeichneten, postsynaptischen Strömen rekonstruiert werden. Beide Methoden deuteten darauf hin, dass in der Präsynapse zwei unterschiedlich schnell fusionierende Populationen synaptischer Vesikel existieren (Abbildung 8A). Experimente mit

Calciumpuffern zeigten ein unterschiedliches Verhalten der Vesikelpopulationen: Schnell fusionierende Vesikel setzten Transmitter auch bei Hinzugabe von Calciumpuffern frei. Calcium erreicht somit unmittelbar nach Durchtritt durch Calciumkanäle das synaptische Vesikel, bevor Calciumpuffer wirksam werden. Eine enge Kopplung zwischen Calciumkanälen und synaptischen Vesikeln könnte dafür verantwortlich sein. Die Fusion von langsam freigesetzten Vesikeln hingegen wurde durch Calciumpuffer verhindert, so dass eine größere Distanz zur Calciumquelle ursächlich sein könnte.

Die Nachladung freigesetzter Vesikel wurde ebenso im Rahmen von Paarableitungen adressiert. Sowohl die Rekonstruktion der Transmitterfreisetzung aus postsynaptischen Strömen (Abbildung 8A), als auch direkte präsynaptischen Kapazitätsmessungen (Abbildung 8B) ergaben bei intensiver Stimulation eine Nachladung von ~400 Vesikeln pro Sekunde und pro Moosfaser-Körnerzell-Synapse. Die Stimulation mit physiologischeren Stimulationsmustern (Abbildung 8D) ergab eine identische Nachladerate. Zudem schien die Nachladung der Vesikel nicht durch Veränderung der präsynaptischen Calciumpuffer beeinflusst zu werden. Dies gibt Hinweise auf eine calciumunabhängige Nachladerate (Abbildung 8 A, B und D). Um die Calciumabhängigkeit der Vesikelnachladung zu verstehen, werden in Zukunft weitere Experimente notwendig sein.

Implikationen für die Signalverarbeitung im Cortex des Kleinhirns

Diese Erkenntnisse lassen Schlüsse zur Funktion der Moosfaser-Körnerzell-Synapse im Netzwerk der Kleinhirnrinde zu. Über Moosfasern werden hochfrequente Aktionspotenziale bis in den Kilohertz-Bereich an die Kleinhirnrinde vermittelt. Diese werden präzise und innerhalb kurzer Zeitfenster über schnelle Ionenkanäle, durch eine enge Kopplung von der Calciumquelle zu den synaptischen Vesikeln und eine schnelle Transmitterfreisetzung auf Körnerzellen übertragen. Dabei integrieren Körnerzellen Signale von bis zu vier Moosfasern. Stochastische Moosfaser-Signale hingegen, die keine Information tragen, werden durch eine tonische Hemmung von Körnerzellen abgeschwächt. Dadurch erfüllen Körnerzellen eine Filterfunktion und diskriminieren Informationen von synaptischem Rauschen. Die engen anatomischen Verhältnisse der Körnerzellschicht und die hohe Divergenz der

Moosfaserboutons machen die Ausbildung von Präsynapsen mit vielen synaptischen Kontakten pro Postsynapse unmöglich. Trotzdem vermitteln Moosfaserboutons über wenige synaptische Kontakte zuverlässig Signale an Körnerzellen. Hierfür sind unter anderem eine schnelle Freisetzung von wenigen synaptischen Vesikeln pro Kontakt und deren schnelle Nachladung verantwortlich. Die Moosfaser-Körnerzell-Synapse wird damit zur kleinstmöglichen physischen Struktur maximaler Moosfaser-Körnerzell-Divergenz (vgl. Eccles *et al.*, 1967).

6 Anlagen

6.1 Supplemental Material

(die Formatierung wurde der Dissertation angepasst)

SUPPLEMENTAL FIGURES

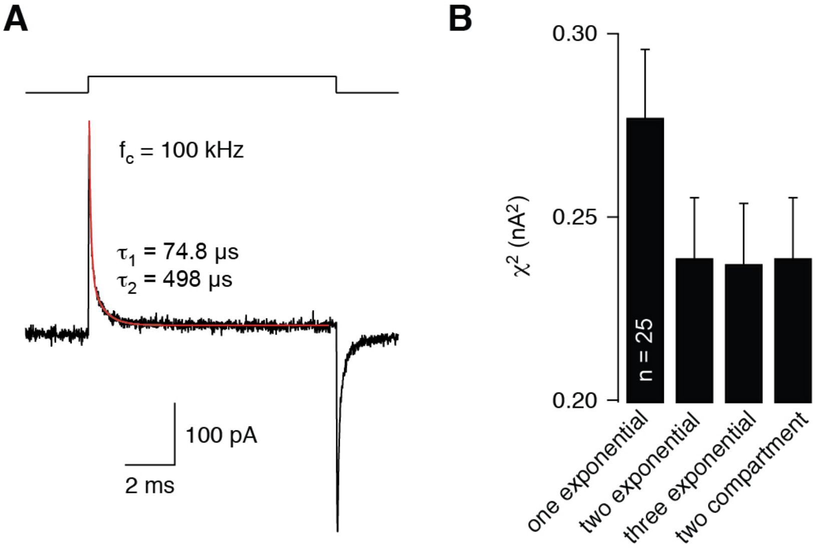

Figure S1 (related to Figure 1). Passive properties of cMFBs

(A) Example trace of passive current transients elicited by +10 mV depolarization from −80 mV holding potential with a filter cut-off frequency (f_c) of 100 kHz (average of 100 consecutive traces) superimposed with a biexponential function (time constants are indicated).

(B) Average sum-of-squared differences (c^2) between data and fitting function. Exponential functions with one, two or three components and a prediction of a two-compartment model (Hallermann et al., 2003) are compared.

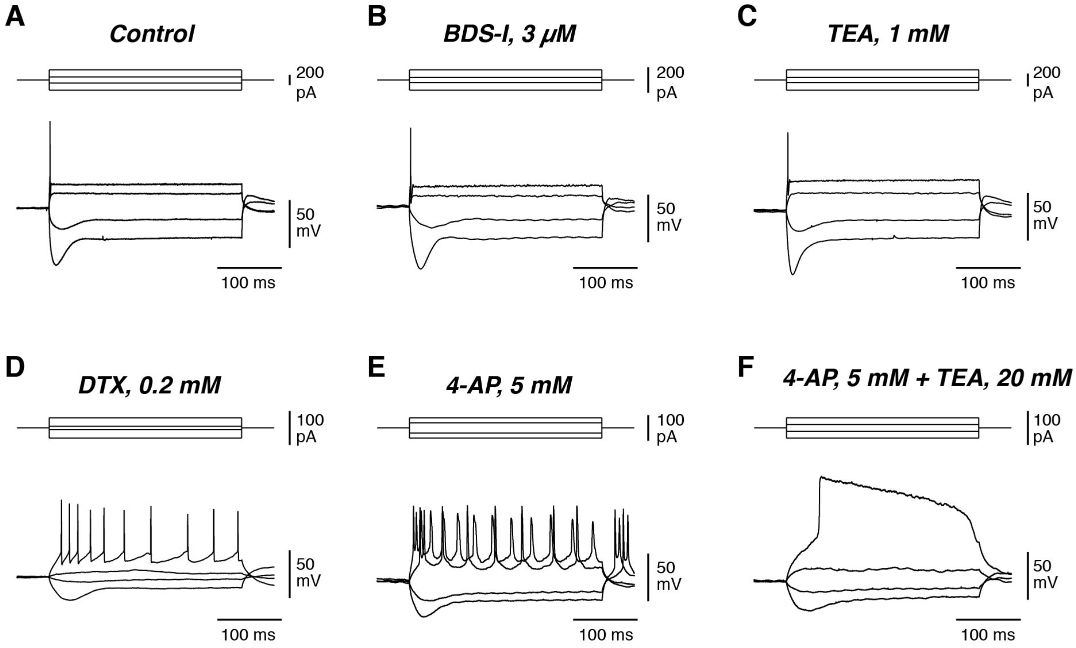

Figure S2 (related to Figure 2). K$^+$ channel subtypes differentially affect cMFBs firing

(A) Voltage responses of cMFBs elicited by tonic current injection (duration, 300 ms) in current-clamp mode. cMFBs fired a single AP upon depolarizing current injection, showed outward rectification, and a time-dependent 'sag' upon hyperpolarizing current injection (Rancz et al., 2007).

(B) Specific blockage of K_{v3} channels by focal application of 3 µM BDS-I resulted in broadening of the AP (cf. Figure 2D) with otherwise unaltered voltage response.

(C) Application of 1 mM TEA had similar effects as focal application of BDS-I.

(D) Blocking K_{v1} channels specifically by 0.2 mM DTX resulted in broadening of the AP and in repetitive firing upon depolarizing current injection.

(E) Application of 5 mM 4-AP had similar effects as DTX.

(F) A combination of 5 mM 4-AP and 20 mM TEA drastically impaired AP repolarization, which was only detectable after the end of tonic current injection, making AP half-duration indeterminable.

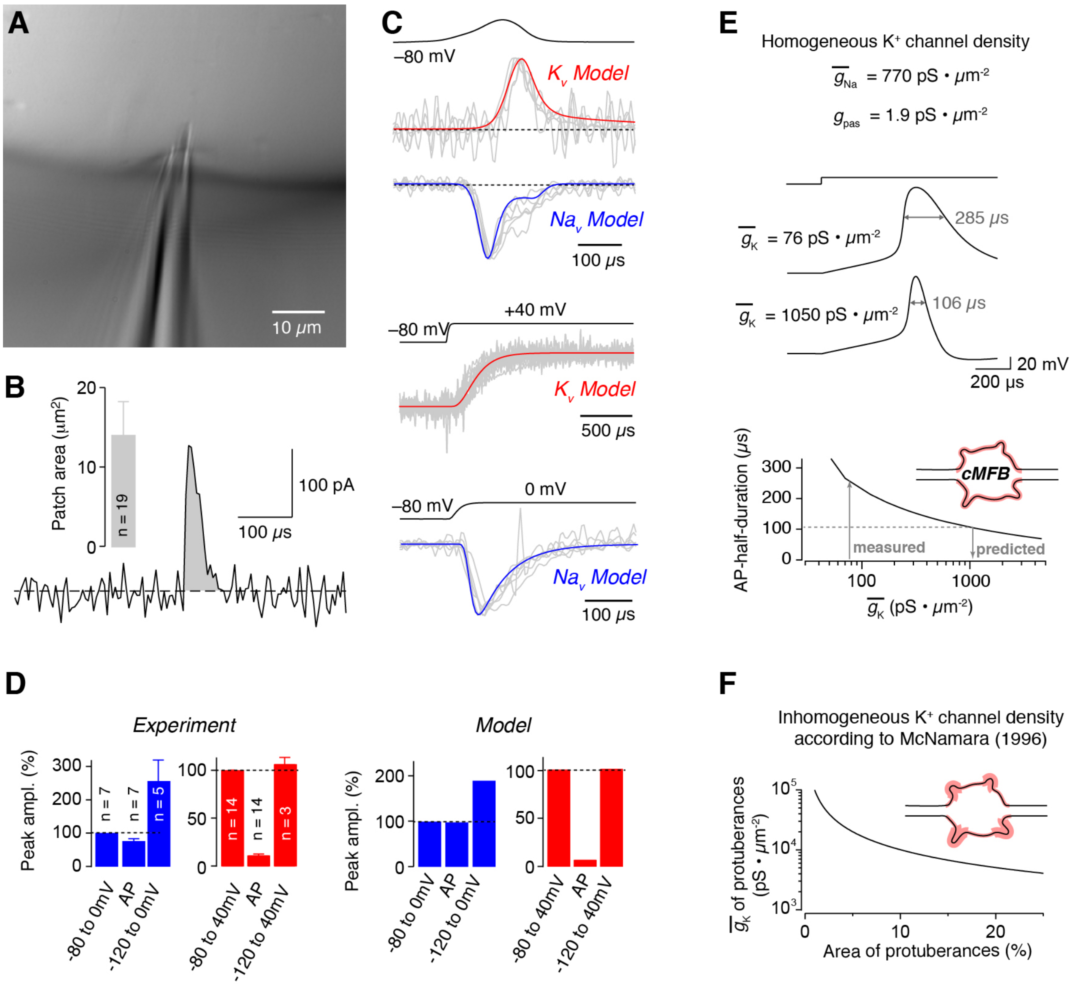

Figure S3 (related to Figure 3). Density estimates from outside-out patches and Hodgkin-Huxley-modeling indicate high density of clustered K^+ channels

(A) Sylgard ball with slightly immerged pipette.

(B) Difference current before and after pressing the pipette tip with the outside-out patch into the Sylgard ball (average of 100 traces each). Grey area indicates integral under the current trace. Currents were evoked by a test pulse to −70 mV from a holding potential of −120 mV.

(C) AP-evoked and step-evoked currents superimposed with predictions of Hodgkin-Huxley models.

(D) Peak current amplitudes measured in outside-out patches (*left*) and predicted by the model (*right*; normalized to the peak amplitude with the step from a holding of −80 mV; average 108 ± 41 pA (n = 7) for Na^+, and 170 ± 37 pA (n = 14) for K^+ currents). Blue and red bars represent data for Na^+- and K^+-channels, respectively.

(E) *Top:* APs predicted by the model with the indicated parameters. *Bottom:* Predicted AP half-duration as a function of $\bar{g}_K$ in the model.

(F) Required $\bar{g}_K$ in protuberances to generate an AP half-duration of 107 µs as a function of the relative area of protuberances.

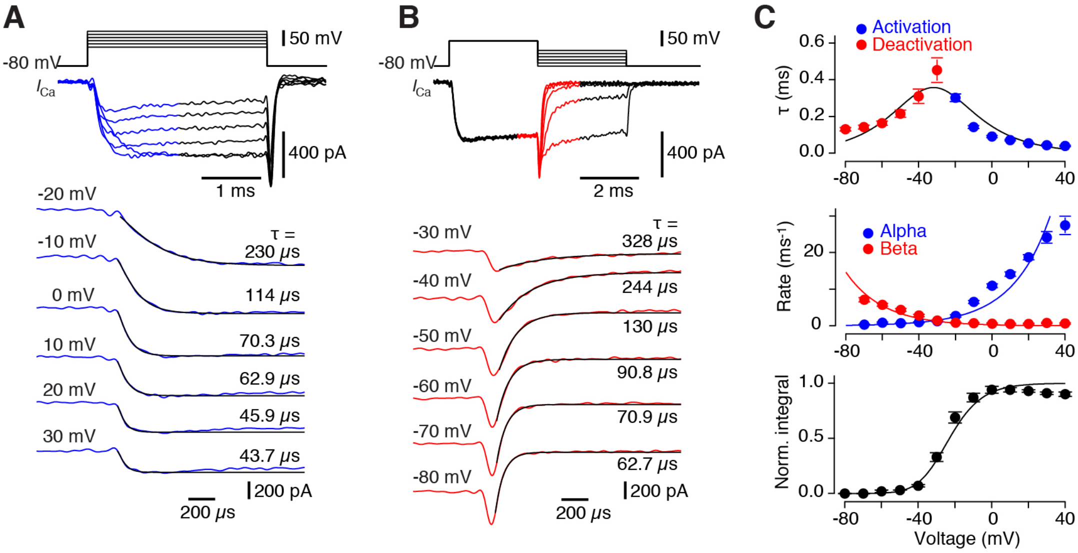

Figure S4 (related to Figure 5). Rapid activation and deactivation of Ca^{2+} channels in cMFBs

(A) *Top:* Example traces of Ca^{2+} currents evoked by voltage steps from −80 mV to +60 mV. Traces of six voltage steps (from −20 mV to +30 mV) are shown. *Below:* Magnification of the onset of Ca^{2+} currents (blue lines above). Ca^{2+} channel activation kinetics was fit with a squared exponential function (black superimposed lines). The activation time constants are indicated.

(B) *Top:* Example traces of Ca^{2+} currents evoked by a voltage step to 0 mV followed by test potentials (from −30 mV to −80 mV). *Below:* Magnification of the deactivating Ca^{2+} currents (red lines above). Ca^{2+} deactivation kinetics was fit with a mono-exponential function (black superimposed lines). The deactivation time constants are indicated.

(C) Top: Activation (blue) and deactivation (red) time constants (n = 14) superimposed with the predictions of a two-gate Hodgkin-Huxley model. *Middle:* Rate constants for opening (alpha) and closing (beta; n = 14; see methods) superimposed with the predictions of a two-gate Hodgkin-Huxley model. *Below:* Tail current integral of the activation traces (n = 14). Data were normalized to the maximum integral and superimposed with the model predictions .

Method	Stimulus	Condition	N_1 (ves)	τ_1 (ms)	N_2 (ves)	τ_2 (ms)	s (ves/s)	Recruitment (Hz)[d]	N_{AP}[e]	n[f]
Deconvolution[a] 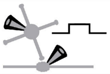	pre-synaptic depolarization	control	15.2 ± 4.3	0.43 ± 0.05	7.3 ± 1.4	5.6 ± 1.4	358 ± 132	24	5.2 ± 1.2	10
		5 mM EGTA	12.5 ± 1.7	0.51 ± 0.03	0.8 ± 0.2	5.6 (fixed)	490 ± 44	39	4.4 ± 1.0	7
Capacitance[b] 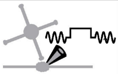		control	6.4	0.43 (fixed)	23.7	6.2	314	50	-	21
		5 mM EGTA	8.1	0.51 (fixed)	-	-	366	45	-	15
Back-extrapolation[c] 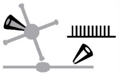	axonal stimulation	pre-wash	13.7 ± 3.4	-	-	-	469 ± 150	34	5.8 ± 0.9	10
		EGTA-AM	10.3 ± 3.0	-	-	-	433 ± 96	42	3.8 ± 0.9	10

Table S1. Parameters of release at cMFBs (related to Figure 8)

[a] For deconvolution experiments (Figure 8A), the cumulative release was fit with the sum of bi-exponential functions and a line. For 5 mM EGTA, t_2 was constrained to the value obtained in control experiments.

[b] For capacitance measurements (Figure 8B), the data were fit with a bi-exponential function and a line for control, and with a mono-exponential function and a line for 5 mM EGTA. The first time constant was constrained to the values obtained with deconvolution experiments, because the shortest duration in the capacitance experiments was 1 ms. The number of vesicles was calculated assuming 70 aF/vesicle (Hallermann et al., 2003) and 100 GC contacts per cMFB (cf. Figure 7C). Compared with estimates from deconvolution analysis, the values are very similar, except for the proportion of fast and slowly releasing vesicles within the pool of release-ready vesicles, which can be explained by the limited temporal resolution of capacitance measurements that is determined by the duration of the depolarizations in these experiments.

[c] For back-extrapolation from train experiments (Figure 8C and D), the amplitude and the slope of the linear back-extrapolation are given before and after application of EGTA-AM.

[d] The recruitment rate was calculated by division of s by N_1.

[e] The quantal content (N_{AP}) was estimated from back-extrapolation experiments by division of evoked and miniature EPSC amplitudes. To estimate N_{AP} from deconvolution experiments, the release during the first 200 μs from the corresponding component of each cell was considered, based on the half-duration of the AP-evoked Ca^{2+} current of ~100 μs (cf. Figure 6) and a delay of the Ca^{2+} current of ~100 μs during step depolarizations (cf. Figure S4; i.e. $N_{AP} = \tau_1 N_1[1 - \text{Exp}(-200\mu s/\tau_1)]$). Note, 5 mM EGTA had no significant effect on the first release component, whereas EGTA-AM reduced EPSC

amplitude by 37% and the number of release-ready vesicles estimated by back-extrapolation by 25% ($p < 0.01$, Wilcoxon signed-rank test; Figure 8D). However, this apparent discrepancy could be explained by an EGTA concentration higher than 5 mM in the EGTA-AM experiments. Also, in deconvolution experiments, 5 mM EGTA had a tendency to reduce N_1 and to increase t_1. Although these changes were not significant, it would predict a reduction in N_{AP} by 29%.

(f) Number of experiments.

SUPPLEMENTAL EXPERIMENTAL PROCEDURES

Passive properties of cMFBs

Passive properties of cMFBs (Figure S1) were analyzed as previously described (Hallermann et al., 2003). Current transients were evoked by square pulses with amplitudes of ±10 mV from a holding potential of −80 mV at a filter cut-off frequency of 100 kHz (three-pole Bessel). Responses to positive and negative pulses were averaged separately (n = 100 traces) and plotted against each other for corresponding time points. Experiments with signs of nonlinearity (slope <0.98 or >1.02) or with access resistance >40 MW were discarded (22 of 47 boutons). Two exponential fits approximated the current transients considerably better than fits with a single exponential function. However, in contrast to hippocampal mossy fiber boutons (Hallermann et al., 2003), three exponential fits were on average only marginally better than two exponential fits (Figure S1). Therefore, a two-compartment model was used (Hallermann et al., 2003). The capacitance and the resistance of the cMFB were 4.0 ± 0.3 pF and 1.3 ± 0.1 GW, respectively. The capacitance and the resistance of the second compartment (most like representing the adjacent axon) were 5.4 ± 0.9 pF and 1.4 ± 0.2 GW, respectively. Both compartments were connected by a resistance of 250 ± 35 MW (n = 25). Including all experiments in the analysis yielded similar results: The capacitance of the first and the second compartment were 3.7 ± 0.2 pF and 5.1 ± 0.6 pF, respectively, and resistance between both compartments was 220 ± 21 MW (n = 47).

Analysis of paired recordings between cMFBs and GC

The synaptic delay (Figure 1C) was determined as the time interval between the maximum of the first derivative of the presynaptic AP and the onset of the EPSC; the onset was determined from the intersection of the preceding baseline with a line through the 20% and 80% points of the EPSC rising phase (Geiger and Jonas, 2000). Phasic EPSC size during kHz transmission (Figure 1D) was measured similarly as described in Hallermann et al. (2010). The peak EPSC amplitude within a window from 0.2 ms to 1 ms was measured relative to a baseline window from −0.4 ms to −0.2 ms (here t = 0 is the beginning of each 200-µs-depolarization of the cMFB to 0 mV).

APs in cMFBs

Amplitudes of APs were measured from threshold (dV/dt >50 V/s) to peak (Kole and Stuart, 2008). The duration of APs was measured at half-maximal amplitude and referred to as half-duration. For axonal stimulation of cMFBs (Figure 2 and 4), the Atto 594 filled axon was approached with a second pipette (~8 MΩ) filled with extracellular solution (stimulation 100 µs, 0.5–10 V). To minimize the stimulation artifact (cf. arrow Figure 2C), the location of stimulation and of the recorded cMFB were separated by more than ~100 µm. Recordings were performed with the EPC10 patch clamp amplifier containing a voltage follower circuit for current clamp recordings (Magistretti et al., 1996). Bridge compensation was not used. The pipette capacitance was compensated in the cell-attached configuration and was minimized for all recordings by filling the pipettes with as little intracellular solution as possible (1–2 mm), and by greasing the silver wires with silicon paste. The access resistance to cMFBs and AP half-duration of cMFBs did not correlate (Pearson's correlation coefficient R = −0.03; p = 0.80).

The contribution of distinct K^+ channel subtypes to AP half-duration was tested by application of K^+ channel blockers (Figure 2D and E). APs were elicited in current clamp mode by tonic current injection in the presence of one of the following combinations of K^+ channel blockers in the extracellular solution: DTX (0.2 mM), TEA (1 mM), 4-AP (5 mM), or 4-AP (5mM) + TEA (20 mM). In addition, BDS-I was focally applied using a second pipette (final BDS-I concentration 3 µM in HEPES-buffered ACSF; Alle et al., 2011; Martina et al., 2007).

Na^+ and K^+ currents in cMFBs

For outside-out patches obtained from cMFBs (Figure 3) open tip pipette resistances ranged from 5–7 MΩ. The internal two-pole Bessel filter for stimulus voltage was set to 20 µs. The resulting voltage commands were sampled from the EPC10 amplifier and shown in Figure 3 and S3 as voltage commands. Currents were low-pass filtered using the 30 kHz internal 3-pole Bessel filter of the EPC10 amplifier and a digital 45 kHz low-pass filter implemented with the finite impulse response filter tool in IGOR Pro, resulting in a −3 dB low-pass cut-off frequency of ~25 kHz (Colquhoun and Sigworth, 1995). Recorded currents were left shifted by 20 µs to account for the delay by the 30 kHz Bessel filter of the current monitor. Na^+ and K^+ currents were corrected for leak and capacitive currents using the P/4-method and represent averages of 20–100 P/4-corrected repetitions. In some of the experiments, small capacitive artifacts remained despite P/4 correction, which decayed to zero before the onset of the Na^+ or K^+ currents (within <25 µs), and were removed by interpolation.

Na^+ and K^+ currents were elicited by an AP waveform voltage-clamp command (Figure 3A-C; Borst and Sakmann, 1998) that was recorded in current-clamp mode with axonal stimulation in a different set of experiments (half-duration 118 µs, amplitude 117 mV; cf. Figure 2C). In addition, currents were evoked by 3-ms depolarizations from −80 mV to 0 mV or 40 mV for Na^+ and K^+, respectively. In a subset of recordings, maximum Na^+ currents were also elicited following a 9-ms prepulse to −120 mV to recover channels from steady-state inactivation. Kinetic analysis was restricted to experiments with optimal signal-to-noise ratio (APs: n = 6 and 5, for Na^+ and K^+; 3-ms: n = 5 and 12, for Na^+ and K^+, respectively; cf. Figure 3). To estimate the recruitment during an AP, the AP-evoked peak current amplitude was normalized to the 3-ms step-evoked peak amplitude (n = 7 and 14, for Na^+ and K^+, respectively; Figure S3D).

Patch-area measurements

Surface area of outside-out patches was determined in a separate set of 19 recordings from GCs. Pipettes had resistances similar to those used for presynaptic current measurements (6–7 MΩ). Outside-out patches were hyperpolarized to −120 mV and subsequently depolarized to −70 mV for 5 ms. Resulting capacitive transients were measured before and after insertion of the pipette tip ~10 mm into a ball of Sylgard®184 (Sigma Aldrich; Figure S3A). In these experiments, pipettes were also coated with Sylgard. Patch size was calculated from integrals under the difference current traces before and after pushing the patch pipette into the Sylgard. Based on a specific membrane capacitance of 1 $fF \cdot mm^{-2}$, the average area was 13.9 ± 4.3 μm^2 (n = 19; Figure S3B), similar to estimates with corresponding pipette resistances (Hu and Jonas, 2014)

Hodgkin-Huxley modeling of cMFB APs

Previously established Hodgkin-Huxley models of axonal Na^+ and K^+ channels (Hallermann et al., 2012) were manually adjusted to reproduce AP- and step-evoked currents (Figure S3C). All rates of the Na^+ channel model, which was originally established for room temperature (Schmidt-Hieber and Bischofberger, 2010), were increased by using a Q_{10} temperature coefficient of 4. To reproduce our K^+ currents, all rates of the K^+ channel model (with 4 activation gates), which was established at 33°C (Hallermann et al., 2012), had to be increased by a factor of 2.3.

The channel models were implemented in the NEURON simulation environment (v7.3) (Carnevale and Hines, 2005) with NEURON extension NMODL, and the currents were calculated in a single compartment that was voltage clamped with an action potential or step waveform, which was sampled after the 20-μs stimulus output filter (cf. voltage command in Figure 3). To model the AP, currents were incorporated in a single compartment model. $\bar{g}_{Na}$ was set to 722 pS·μm^{-2}, based on 276 pA peak current amplitude with steps from −120 to 0 mV (Figure S3D), a driving force of 55 mV (+55 mV reversal potential), and a patch area of 13.9 μm^2 (Figure S3B). Furthermore, a factor of 2 was used to account for the reduced peak amplitude due to Na^+ inactivation (Schmidt-Hieber and Bischofberger, 2010). $\bar{g}_K$ was correspondingly calculated to be 82 pS·μm^{-2}, based on 175 pA peak current amplitude with steps from −120 to +40 mV (Figure S3D), a driving force of 140 mV (−100 mV reversal potential), and a patch area of 13.9 μm^2. In addition, a leak conductance (1.9 pS·μm^{-2}, reversal 0 mV) was added based on 1.3 GW and 4 pF of the first compartment of the passive model of the cMFB (cf. Figure S1).

With these values the model predicted a too long AP half-duration of 265 μs (Figure S3E). To obtain the measured half-duration of 107 μs, $\bar{g}_K$ had to be increased to 1050 pS·μm^{-2}. We obtained similar results with several other published models of K^+ channels, which were adjusted to reproduce our gating kinetics (Figure S3C), indicating that the exact voltage dependence of the K^+ channel model has minor impact on this result. Furthermore, variations in $\bar{g}_{Na}$ or the size of the leak conductance had little effect on the predicted half-duration.

Interestingly, one in 15 outside-out patches, in which K^+ currents were recorded, had 20-fold higher current amplitude but normal kinetics with both the AP- and 3-ms-voltage command. It was excluded from the analysis because the amplitudes differed from the mean by 25-fold the standard deviation, but it may represent a recording from a K^+-channel-rich membrane area. Finally, we varied the proportion of the area of the protuberances and calculated the required K^+ current density of the protuberances (Figure S3F). With an area of 10%, a $\bar{g}_K$ of 10,000 pS·µm^{-2} is predicted for the protuberances.

Ca^{2+} currents

Presynaptic Ca^{2+} currents were pharmacologically isolated during cMFB whole cell patch-clamp recordings (see *Methods*, section solutions). For a maximal resolution of fast current kinetics, patch pipettes with least practicable pipette resistances (R_{pip} = 3–4 MW) were used. In these experiments, our time constant of the voltage clamp was in the range of 40 µs (assuming 10 MW access resistance and 4 pF cMFB capacitance; cf. Figure S1), which was similar to our filter characteristics (10 kHz resulting in a 10–90% rise time of 33 µs; Colquhoun and Sigworth, 1995). The activation kinetics of Ca^{2+} currents in cMFBs evoked at 0 mV was 90 ± 18 µs (n = 13; Figure S4C), significantly above the temporal resolution of the experimental conditions (40 µs). However, at more depolarized potentials the recorded kinetics might be limited by resolution and therefore activation might be even faster. Ca^{2+} currents were elicited by an AP waveform voltage-clamp command (see above), by square pulses of 3 ms duration (Figure S4), and by mock APs (Figure 5B; Wheeler et al., 1996). Mock APs were composed of a ramp (100 µs, from −80 to +40 mV) followed by a plateau of increasing durations (+40 mV; 40, 80, 160, 320, 640, 1280 µs) and a 60-µs-ramp to the holding potential of −80 mV. Ca^{2+} currents were corrected for leak and capacitive currents using the P/4-method.

To construct a two-gate Hodgkin-Huxley model for the Ca^{2+} channels in cMFBs (m^2; Hodgkin and Huxley, 1952; Figure S4C), we essentially followed a previously described approach (Lin et al., 2011). Activation of Ca^{2+} current was measured during steps from −80 mV to potentials between −20 and +30 mV. Integrals of the Ca^{2+} tail currents (500 µs) were used as a measure for steady-state activation (m_∞) after normalization to the peak value and taking the square root. The time course of current activation (0–1.5 ms after pulse onset) was fit with a squared exponential function with delayed onset and a time constant t_m:

$$I(t) = I_\infty(1 - \exp(-(t - t_0)/\tau_m))^2$$

Deactivation of Ca^{2+} current was measured during steps from 0 mV to voltages between −30 and −80 mV, which were fit with single exponentials. The obtained time constants from exponential fits to the tail currents (t_e) were then used to approximate the time constants of relaxation of the gate (t_m) after a voltage step using the following expression (Hagiwara and Ohmori, 1982):

$$\tau_m = \tau_e * 2m_0/(m_0 + m_\infty)$$

where m_0 and m_∞ represent the values of the steady state activation curve of each cMFB at −80mV and at the potential of the deactivation step, respectively. The rate constants were calculated as $\alpha_m = m_\infty/\tau_m$, and $\beta_m = (1 - m_\infty)/\tau_m$. Rate constants a_m and b_m of the Hodgkin-Huxley model were defined as:

$$\alpha_m = \alpha_0 * \exp(V_m/V_\alpha)$$

$$\beta_m = \beta_0 * \exp(-V_m/V_\beta)$$

Finally, the free parameters of the model were determined by minimizing the deviation of the model from the data with the FindMinimum routine of Mathematica 9.0. The deviation of the model from the experiments was measured as the sum of squared differences for the time constants of activation and inactivation (in ms), the rates a_m and b_m (in ms^{-1}; weighted by 10^{-1}) and the steady-state activation (cf. Figure S4C). The resulting best-fit parameters were α_0 = 6.52 ms^{-1}, V_α = 20.8 mV, β_0 = 0.288 ms^{-1}, and V_β = 20.4 mV. The results were independent of the starting values in a plausible range.

To calculate the Ca^{2+} current based on the AP voltage command (Figure 5A), the differential equation

$$\frac{dm}{dt} = \alpha_0(1 - m) - \beta_m\, m$$

was solved numerically with the NDSolve function of Mathematica and a three-order polynomial interpolation of the AP-voltage command was used as V_m(t). Finally, the Ca^{2+} current was calculated as $I(t) = m(t)^2(V(t) - V_{rev})$, where V_{rev} is the assumed reversal potential of +50 mV.

Ca^{2+} channel subtypes

To determine the contribution of different voltage-gated Ca^{2+} channel subtypes in cMFBs (Figure 6A and B), $Ca_v2.1$, $Ca_v2.2$, and $Ca_v2.3$ Ca^{2+} channels were specifically blocked in whole-cell patch-clamped cMFBs by bath application of w-Agatoxin IVa (0.5 µM, from Bachem, Bubendorf, Switzerland), w-Conotoxin GVIa (1 µM, from Bachem, Bubendorf, Switzerland), or SNX-482 (0.5 µM, from Peptides International, Louisville, USA), respectively. Holding potential was −80 mV during recordings. Ca^{2+} currents were evoked by 3-ms depolarizing pulses to 0 mV, applied at a frequency of 0.1 Hz. Ca^{2+} current amplitude was measured during steady-state. Following a control period of ~200 s, a subtype specific toxin was applied to the bath solution. After the decrease in Ca^{2+} current amplitude had reached a plateau level, a second blocker was applied. The order of toxins was varied between recordings. In some recordings only a single toxin was used. To account for rundown of Ca^{2+} currents, the initial reduction of Ca^{2+} current amplitude was fit with an exponential function (Figure 6A). On average, the steady-state value of this function was 64 ± 4% (n = 17) of the initial amplitude, including experiments without any toxin application, indicating rundown of 36% during these Ca^{2+} current recordings. In addition, after each toxin application the Ca^{2+} current amplitude was fit with an exponential function. The inhibition by w-Agatoxin, w-Conotoxin, and SNX was quantified as difference between the steady-state values of the corresponding exponential functions normalized to the steady-state values without toxin application.

Immunoelectron microscopy

Preembedding immunogold labeling (Figure 6C) was performed as described (Kaufmann et al., 2013). Briefly, adult C57Bl/6 mice were anesthetized with sodium pentobarbital (50 mg/kg, i.p.) and perfused transcardially with a fixative containing 4% formaldehyde, 0.05% glutaraldehyde and 15% of a saturated picric acid in 0.1 M phosphate buffer (PB, pH 7.4). Parasagittal sections were cut at 50 mm, cryoprotected with 20% sucrose, flash frozen on liquid nitrogen and rapidly thawed. Sections were then incubated in 10% normal goat serum (NGS) and 2% bovine serum albumin (BSA) in Tris-buffered saline (TBS) for 2 h at room temperature, incubated in TBS containing 2% BSA and guinea pig anti-$Ca_v2.1$ antibody (1 mg/ml, Indriati et al., 2013) for 48 h at 4°C, and finally reacted with nanogold-conjugated secondary antibody (Nanoprobes, 1:100) for 24 h at 4°C. Nanogold particles were amplified with HQ Silver Enhancement kit (Nanoprobes) for 10 min. Sections were then treated in 2% osmium tetroxide in PB for 40 min, 1% uranyl acetate in 50% ethanol for 30 min at room temperature, dehydrated, and flat embedded in Drucupan resin (Sigma-Aldrich). Ultrathin sections were cut at 70 nm and observed by a transmission electron microscope (Tecnai 12, FEI, Oregon).

For the quantitative analysis of synaptic and extrasynaptic immunogold particle labeling (Figure 6D), 18 images of mossy fiber terminals covering 3.8 x 3.8 μm area each at a magnification of 26,500 were recorded using VELETA CCD camera (Olympus) and analyzed with iTEM software (Olympus Soft Imaging Solutions GmbH, Münster). Synapses were defined as areas with presynaptic vesicle accumulation, postsynaptic density, rigid alignment of pre- and postsynaptic membranes and electron-dense materials in the cleft. Total length of 9.29 μm and 251.08 μm were analyzed for synaptic (n=53 synapses) and extrasynaptic membrane, respectively. Immunogold particles within 30 nm from the edge of presynaptic membranes were included in the analysis based on the possible distance of the immunogold particle from the epitope (Matsubara et al., 1996).

Freeze-fracture replica labeling (SDS-FRL; Figure 6E) was performed as described previously (Indriati et al., 2013). The mice were perfused with 2% paraformaldehyde (PFA) with 15% saturated picric acid solution in 0.1 M PB. Parasagittal slices (130 μm thick) were cut using a vibrating microslicer (Linear-Pro7, Dosaka, Kyoto) and middle lobules of cerebellar slices were trimmed, immersed in graded glycerol of 10–30% in 0.1 M PB at 4°C overnight, and then rapidly frozen by a high pressure freezing machine (HPM010, BAL-TEC, Balzers). Frozen samples were fractured into two parts at −140°C and replicated by deposition of carbon (2 nm thick), platinum/carbon (uni-direction from 60°, 2 nm) and carbon (15 nm) in a freeze-fracture replica device (JFD II, JEOL, Tokyo). Tissue debris was dissolved in a solution containing 15 mM Tris-HCl (pH 8.3), 20% sucrose, and 2.5% SDS with gentle shaking at 80°C for 18 h. The replicas were washed three times in washing buffer containing 0.05% BSA in 50 mM TBS and blocked with 5% BSA in the washing buffer for 1h at room temperature. The replicas were then incubated with the $Ca_v2.1$ antibody (8.1 µg/ml) overnight at 15°C followed by incubation with 5 nm gold conjugated anti-guinea pig secondary antibodies (British Biocell International (BBI), Cardiff) overnight at 15°C. The specificity the $Ca_v2.1$ immunolabeling was confirmed by testing cerebellar tissues from $Ca_v2.1$ KO mice (Indriati et al., 2013).

Capacitance recordings

Capacitance measurements (Figure 7 and 8) were performed with sine-wave stimulation (1 kHz, amplitude ±50 mV, holding potential −100 mV) essentially as described previously (Hallermann et al., 2003). In between sine-wave stimulation, the presynaptic terminal was depolarized from −80 mV to 0 mV for 1–100 ms. The capacitance increase was determined as the difference between the mean capacitance 50–100 ms after the depolarizing pulse and the average baseline during 50 ms before onset of the depolarizing pulse.

Deconvolution

Deconvolution of postsynaptic currents (Figure 7 and 8) was performed essentially as described by Neher and Sakaba (2001). This method is based on the assumption that the postsynaptic current is a sum of current induced by synchronous release and residual current caused by residual glutamate in the synaptic cleft, part of which might result from glutamate spillover onto neighboring active zones. The amplitude of the miniature EPSC (mEPSC) was set to the mean value measured in 1 mM kynurenic acid and 100 µM cyclothiazide (14.2 ± 0.9 pA; n = 21). To determine the free parameters of the model, i.e. the mEPSC risetime t_0, the fractional amplitude of the slow mEPSC decay phase a, the time constant of the slow component of decay t_2, the residual current weighting factor b, the diffusion exponent n_D, and the mean diffusional distance r_D, a voltage command protocol similar to the “fitting protocol” described by Neher and Sakaba (2001) was used: after establishing a paired configuration, the presynaptic terminal was depolarized to 0 mV consecutively for 1, 3, 10, 30 and 100 ms and the resulting EPSCs were measured in the postsynaptic cell. Deconvolution was first performed with a set of trial parameters for each cell pair. The parameters of the deconvolution were then optimized consecutively to yield low (but non-negative) release rates after the pulses. For longer pulses (30 and 100 ms), the release rate sometimes remained elevated for a few milliseconds after the depolarization, probably due to an increase in intracellular Ca^{2+}. These experiments were not excluded from the analysis if the same phenomenon also occurred in the simultaneously measured capacitance trace. First, the short pulses (1 and 3 ms) were used to optimize the parameters of the mEPSC, t_0, a and t_2, because there is little residual glutamate build-up during these stimuli. Afterwards, the parameters of the glutamate diffusion model were optimized by fitting the EPSCs of the longer pulses. The resulting cumulative release rates were overlaid with simultaneously measured presynaptic capacitance to further validate the quality of the deconvolution results. In order to correlate the two release estimates, the presynaptic capacitance increase measured in the whole terminal was scaled by a variable factor representing the number of GCs connected by one MFB. The total number of vesicles released during each of these pulses was plotted against the capacitance increase measured in the presynaptic terminal during the pulse and the result could be fit well with a line. The number of MF-GC connections per bouton was determined from the slope of this line, assuming a capacitance of 70 aF/vesicle (Hallermann et al., 2003). Glutamate spillover might compromise the validity of this estimate, because EPSCs could be influenced by spillover, while capacitance recordings are presynaptic and therefore unaffected by spillover. However, spillover is likely to contribute to the residual current, which was subtracted from the EPSC in the deconvolution procedure. The release rates estimated from deconvolution of postsynaptic currents should therefore also be independent of glutamate spillover.

After finding a set of parameters that could well describe the experimental data at an individual connection, we varied the deconvolution parameters by ± 20% to test the robustness of our results. This usually affected the results of the fits to the cumulative release rate by less than 10%. In those cases where the effect was >20%, there were obvious shortcomings in the deconvolution (e.g., negative release rates), which could not be compensated by changing either of the remaining parameters. Once the parameters were determined for a given pair, the same parameters were used for deconvolution of other traces of the same pair.

Kinetics of vesicle release

To determine the kinetics of vesicle release (Figure 8), the cumulative release rates of the 30-ms and 100-ms pulses calculated by deconvolution were first fit with an exponential function and a line according to a model of one vesicle pool with homogeneous release probability and linear vesicle recruitment. However, this fit poorly represented the data in the control experiments during the initial release phase. Therefore, we fit the cumulative release with the sum of two exponential functions and a line according to a two-pool model with different release probabilities and linear vesicle recruitment. These fits represented the initial release phase in the controls considerably better (Figure 8A). Since in experiments with 5 mM EGTA, the initial release appeared mono-exponential, we constrained t_2 in these experiments to the value obtained in control (5.2 ms). Correspondingly, the average capacitance increase plotted versus duration of depolarization was fit with the sum of two exponential functions and a line for control and the sum of one exponential function and a line for 5 mM EGTA, weighted with the inverse of the standard deviation.

EPSC recordings during train stimulation (Figure 8D and C) were performed as previously described (Hallermann et al., 2010). 300 Hz trains (20 stimuli) were applied every 30 s. After 10 min, either EGTA-AM (100 µM, dissolved in DMSO, final DMSO concentration 0.1%) or DMSO alone (for control experiments) was added to the bath perfusion. For evaluation, currents preceding the bath application were averaged and compared to those following application. For DMSO, no effects on first EPSC amplitude or on the time course of depression during the train were observed (data not shown). The number of release-ready vesicles was estimated by back-extrapolation of the cumulated EPSC amplitude essentially as previously described (Schneggenburger et al., 1999): A line was fit to the last 7 of the 20 pulses of the cumulative EPSC amplitude during the 300 Hz train. Extrapolation of this line to t = 0 and division by the average mEPSC amplitude yielded an estimate for the initial number of release-ready vesicles before onset of the stimulation. The slope of the line gave an estimate for the vesicle recruitment rate during the train. The mEPSC amplitude was determined in these experiments to 21.5 ± 2.0 pA (n = 10) from spontaneous EPSCs with a template matching algorithm implemented in Neuromatic software (www.neuromatic.thinkrandom.com). The number of release-ready vesicles and the slope were corrected for a reduction of the mEPSC amplitude to 69% during a 300 Hz train (Hallermann et al., 2010).

Solutions

The extracellular solution contained (in mM): NaCl 125, KCl 2.5, NaH_2PO_4 1.25, $NaHCO_3$ 25, glucose 20, $CaCl_2$ 2, $MgCl_2$ 1. The intracellular solution used for recordings of presynaptic APs, action currents, passive transients, Na^+ and K^+ currents, or postsynaptic EPSCs contained (in mM): K-gluconate 150, Mg-ATP 3, Na-GTP 0.3, K-Hepes 10, NaCl 10, EGTA 0.05 or 0.2. For the EPSC recordings shown in Figure 1 and 8C and D, 10 µM APV was added to the extracellular solution. To isolate K^+ currents (Figure 3), TTX (1 µM) and $CdCl_2$ (100 µM) were added to the extracellular solution. Na^+ currents (Figure 3) were isolated by using the following extracellular solution (in mM): NaCl 105, KCl 2.5, NaH_2PO_4 1.25, $NaHCO_3$ 25, glucose 25, $CaCl_2$ 2, $MgCl_2$ 1, 4-AP 5, TEA 20, XE991 0.01, ZD-7285 0.02, and $CdCl_2$ 0.1. To isolate presynaptic Ca^{2+} currents, to perform capacitance measurements, and to perform deconvolution experiments (Figures 5–7, 8A and B, and S4), the extracellular solution contained (in mM): NaCl 105, KCl 2.5, NaH_2PO_4 1.25, $NaHCO_3$ 25, glucose 25, $CaCl_2$ 2, $MgCl_2$ 1, TTX 0.001, 4-AP 5 and TEA 20; and the intracellular presynaptic patch pipette contained (in mM): CsCl 135, TEA-Cl 20, MgATP 4, NaGTP 0.3, Na_2Phosphocreatine 5, Hepes 10, EGTA 0.2 or 5. For deconvolution of postsynaptic currents (Figure 7 und 8A), 100 µM Cyclothiazide and 1 mM kynurenic acid were added to the extracellular solution to prevent postsynaptic AMPA receptor desensitization and saturation. Chemicals were obtained from Sigma-Aldrich unless otherwise stated.

SUPPLEMENTAL REFERENCES

Carnevale, N.T., and Hines, M.L. (2005). The NEURON book (Cambridge: Cambridge University Press).

Colquhoun, D., and Sigworth, F.J. (1995). Fitting and statistical analysis of single-channel records. In Single-Channel Recording, B. Sakmann, and E. Neher, eds. (New York: Plenum Press), pp. 483-587.

Hagiwara, S., and Ohmori, H. (1982). Studies of calcium channels in rat clonal pituitary cells with patch electrode voltage clamp. J. Physiol. *331*, 231-252.

Hodgkin, A.L., and Huxley, A.F. (1952). A quantitative description of membrane current and its application to conduction and excitation in nerve. J. Physiol. *117*, 500-544.

Kaufmann, W.A., Matsui, K., Jeromin, A., Nerbonne, J.M., and Ferraguti, F. (2013). Kv4.2 potassium channels segregate to extrasynaptic domains and influence intrasynaptic NMDA receptor NR2B subunit expression. Brain Struct. Funct. *218*, 1115-1132.

Kole, M.H.P., and Stuart, G.J. (2008). Is action potential threshold lowest in the axon? Nat. Neurosci. *11*, 1253-1255.

Magistretti, J., Mantegazza, M., Guatteo, E., and Wanke, E. (1996). Action potentials recorded with patch-clamp amplifiers: are they genuine? Trends Neurosci. *19*, 530-534.

Matsubara, A., Laake, J. H., Davanger, S., Usami, S., Ottersen, O. P. (1996). Organization of AMPA receptor subunits at a glutamate synaptse: a quantitative immunogold analysis of hair cell synapses in the rat organ of Corti. J. Neurosci. *16*, 4457-4467.

Neher, E., and Sakaba, T. (2001). Combining deconvolution and noise analysis for the estimation of transmitter release rates at the calyx of held. J. Neurosci. *21*, 444-461.

Schmidt-Hieber, C., and Bischofberger, J. (2010). Fast Sodium Channel Gating Supports Localized and Efficient Axonal Action Potential Initiation. J. Neurosci.*30*, 10233-10242.

Wheeler, D.B., Randall, A., and Tsien, R.W. (1996). Changes in action potential duration alter reliance of excitatory synaptic transmission on multiple types of Ca^{2+} channels in rat hippocampus. J. Neurosci. *16*, 2226-2237.

6.2 Erklärung über den wissenschaftlichen Beitrag des Promovenden zur Publikation

Diese von mir, Andreas Ritzau-Jost, angefertigte Dissertation beruht insbesondere auf Ergebnissen, die zu folgender wissenschaftlicher Veröffentlichung beitrugen:

Ritzau-Jost A, Delvendahl I, Rings A, Byczkowicz N, Harada H, Shigemoto R, Hirrlinger J, Eilers J, Hallermann S (2014) Ultrafast action potentials mediate kilohertz signaling at a central synapse. Neuron 84:152-163.

Ich arbeite seit Februar 2011 im Carl-Ludwig-Institut für Physiologie in Leipzig. Innerhalb von wenigen Monaten war ich in der Lage, routinemäßig *patch-clamp*-Ableitungen von Körnerzellen in akuten Hirnschnitten der Maus eigenständig durchzuführen. Anschließend war ich daran beteiligt, präsynaptische Messungen an cMFBs im Labor von Herrn Prof. Dr. Hallermann zu etablieren und Paarableitungen in der untersuchten Synapse erstmals durchzuführen. Die den folgenden Abbildungen zugrundeliegenden Daten habe ich selbst zum Großteil erhoben: Abb. 1 C,D; Abb. 5; Abb. 7 und Abb. 8. Auch an der Gewinnung der restlichen Befunde war ich beteiligt. Insgesamt führte ich einen großen Teil der Experimente in diesem Manuskript, insbesondere die meisten der äußerst anspruchsvollen Paarableitungen, eigenständig durch. Ich war außerdem in die Planung und die Analyse der Experimente eingebunden, wobei ich, abgesehen von den Deconvolutionsanalysen, die Experimente größtenteils selbstständig auswertete. Zudem habe ich an der Entstehung der Veröffentlichung mitgewirkt, indem ich Textentwürfe verfasst, Abbildungen entworfen und die Auswahl der zu zitierenden Literatur diskutiert habe. Zusammenfassend habe ich einen wichtigen Beitrag zur Entstehung dieser Arbeit geleistet.

Prof. Dr .Stefan Hallermann	Prof. Dr. Jens Eilers
Dr. Igor Delvendahl	Niklas Byczkowicz

6.3 Selbstständigkeitserklärung

Hiermit erkläre ich, dass ich die vorliegende Arbeit selbstständig und ohne unzulässige Hilfe oder Benutzung anderer als der angegebenen Hilfsmittel angefertigt habe. Ich versichere, dass Dritte von mir weder unmittelbar noch mittelbar geldwerte Leistungen für Arbeiten erhalten haben, die im Zusammenhang mit dem Inhalt der vorgelegten Dissertation stehen, und dass die vorgelegte Arbeit weder im Inland noch im Ausland in gleicher oder ähnlicher Form einer anderen Prüfungsbehörde zum Zweck einer Promotion oder eines anderen Prüfungsverfahrens vorgelegt wurde. Alles aus anderen Quellen und von anderen Personen übernommene Material, das in der Arbeit verwendet wurde oder auf das direkt Bezug genommen wird, wurde als solches kenntlich gemacht. Insbesondere wurden alle Personen genannt, die direkt an der Entstehung der vorliegenden Arbeit beteiligt waren.

....

Datum Unterschrift

6.4 Lebenslauf

Angaben zur Person

Familienname:	Ritzau-Jost, geboren Ritzau
Vorname:	Andreas
Geburtsdatum:	31. Oktober 1989
Geburtsort:	Friedrichroda

Schulbildung und Studium

1996 – 2000	Grundschule, Witterda
2000 – 2008	Albert-Schweitzer-Gymnasium, Erfurt
Mai 2008	Allgemeine Hochschulreife / Abitur
2008 – 2015	Studium der Humanmedizin an der Universität Leipzig
2014 – 2015	Auslandsaufenthalt an der Peking University, Peking, China

Klinische Ausbildung

2008 – 2010	Hals-Nasen-Ohren-Heilkunde, Helios Klinikum Erfurt (90-tägiges Pflegepraktikum)
2012	Neurochirurgie, Helios Klinikum Erfurt (Famulatur)
2013	Gastroenterologie, Diakonissenkrankenhaus, Leipzig (Famulatur)
2013	Notfallaufnahme, Asklepios Klinik Wandsbek, Hamburg (Famulatur)

Wissenschaftliche Arbeit

Seit 2011	Studien zu Mechanismen hochfrequenter synaptischer Übertragung, Carl-Ludwig-Institut für Physiologie, Universität Leipzig
2012	Studentische Hilfskraft am European Neuroscience Institute Göttingen, Arbeitsgruppe *high-frequency signalling*

Ausgewählte wissenschaftliche Präsentationen

Ritzau-Jost A, Rings A, Hirrlinger J, Schmidt H, Eilers J, Hallermann S, Mechanisms of high-frequency synaptic transmission at a central excitatory synapse, Presentation number 081, 91. Jahrestagung der Deutschen Physiologischen Gesellschaft (2012), Dresden, Deutschland

Ritzau-Jost A, Delvendahl I, Rings A, Hirrlinger J, Eilers J and Hallermann S, Mechanisms of high-frequency synaptic transmission at a central excitatory synapse, Jahrestagung der Society for Neuroscience (2013), San Diego, USA

Ritzau-Jost A, Delvendahl I, Rings A, Hirrlinger J, Eilers J and Hallermann S, Mechanisms of high-frequency synaptic transmission at a central excitatory synapse, 4th European Synapses Meeting (2013), Bordeaux, Frankreich

Stipendien

2011 – 2012	Promotionsstipendium der Medizinischen Fakultät, Universität Leipzig
2011 – 2015	Stipendiat der Studienstiftung des deutschen Volkes
2014 – 2015	China-Stipendium der Studienstiftung des deutschen Volkes und der Alfried Krupp von Bohlen und Halbach-Stiftung

Mitgliedschaften

Deutsche Physiologische Gesellschaft
Deutsche Neurowissenschaftliche Gesellschaft
Deutsche Gesellschaft für die Vereinten Nationen

Fremdsprachenkenntnisse

Englisch: fließend in Wort und Schrift
Chinesisch: mittleres Sprachniveau
Latein und Französisch: Grundkenntnisse

Interessen

Imkerei, Klettersport, Segeln, Klavierspiel

6.5 Publikationen

Ritzau-Jost A, Delvendahl I, Rings A, Byczkowicz N, Harada H, Shigemoto R, Hirrlinger J, Eilers J, Hallermann S (2014) Ultrafast action potentials mediate kilohertz signaling at a central synapse. Neuron 84:152-163.

Delvendahl I, Weyhersmuller A, **Ritzau-Jost A**, Hallermann S (2013) Hippocampal and cerebellar mossy fibre boutons - same name, different function. J Physiol 591:3179-88.

6.6 Danksagung

Herr Prof. Dr. Stefan Hallermann ist im Laufe meiner Promotion über die Rolle eines Doktorvaters hinaus zu meinem wissenschaftlichen Mentor geworden, dessen uneingeschränktes Engagement zweifelsohne grundlegend für das Gelingen meiner Promotion gewesen ist. Seine hervorragende Betreuung und seine wissenschaftliche Exzellenz haben in jeder Hinsicht zu einer Weiterentwicklung meines wissenschaftlichen Interesses geführt. Unsere Freundschaft ist für mich Leitbild eines offenen und vertrauensvollen Umgangs geworden.

Herrn Dr. Igor Delvendahl gilt ebenso besonderer Dank für unsere enge Zusammenarbeit – sowohl wissenschaftlich, als auch darüber hinaus. Unser freundschaftlicher Umgang und viele spannende Gespräche haben für mich Freude am täglichen Arbeiten geschaffen und meinen Horizont vielfach erweitert.

Frau Dr. Annika Rings möchte ich neben der mir entgegengebrachten Unterstützung, besonders bei der Auswertung experimenteller Daten, ebenso wie Herrn Niklas Byczkowicz für die professionelle Zusammenarbeit danken.

Ich danke Herrn Prof. Dr. Jens Eilers für die Möglichkeit, meine Dissertation in seinem Labor zu beginnen, sowie die Unterstützung, die er mir über den gesamten Zeitraum meiner Arbeit am Carl-Ludwig-Institut entgegengebracht hat – vielfach auch über Themen meiner Dissertation hinaus.

Herrn Prof. Dr. Johannes Hirrlinger, Herrn Priv.-Doz. Dr. Hartmut Schmidt sowie allen weiteren Mitarbeitern des Carl-Ludwig-Instituts danke ich für die angenehme Arbeitsatmosphäre und die vertrauensvolle Aufnahme in die Arbeitsgruppe.

Prof. Dr. Erwin Neher gilt mein Dank für die wertvolle, kritische Auseinandersetzung mit wissenschaftlichen Fragestellungen meiner Promotion und seine methodische Hilfestellung, insbesondere bei der Anwendung der Deconvolution postsynaptischer Ströme.

Ich danke Frau Gudrun Bethge, die mir durch ihre vielfältige und in diesem Umfang nicht selbstverständliche Hilfsbereitschaft die Tätigkeit im Labor nähergebracht hat, Frau Doris Grießhammer für die Unterstützung bei technischen Fragestellungen und Frau Beate Tänzer für ihre ständige Hilfsbereitschaft bei administrativen Fragen.

Der Medizinischen Fakultät der Universität Leipzig danke ich für das großzügige Promotionsstipendium, mit dem sie meine Promotion unterstützte.

Meiner Familie möchte ich für den bedingungslosen Rückhalt in jeder Situation und den vielfachen guten Rat danken.